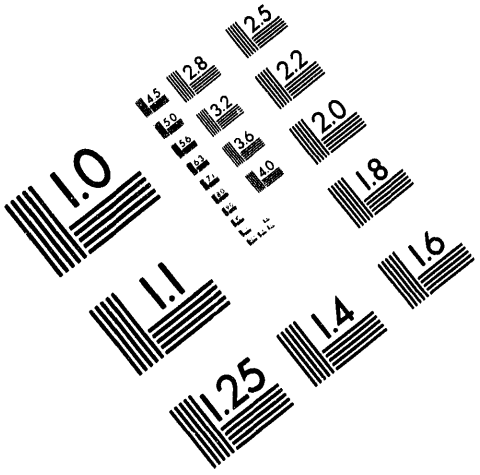

Association for Information and Image Management
1100 Wayne Avenue, Suite 1100
Silver Spring, Maryland 20910
301/587-8202

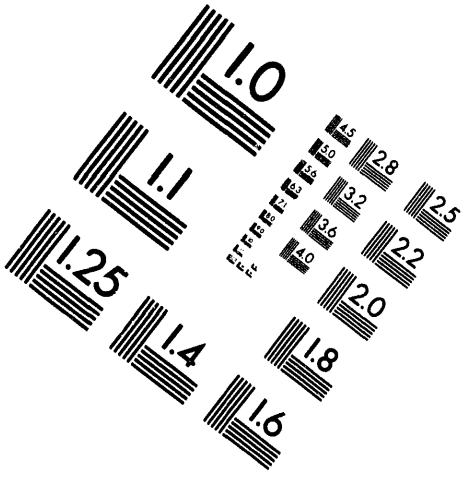

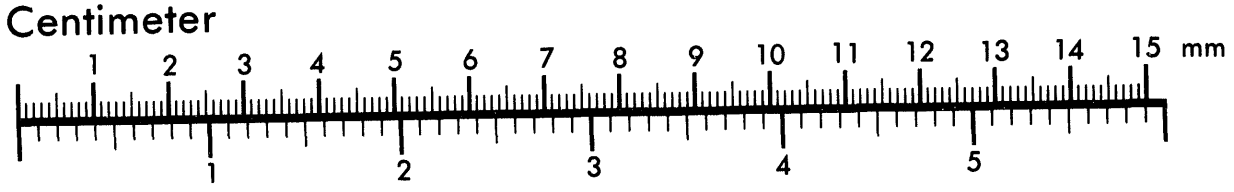

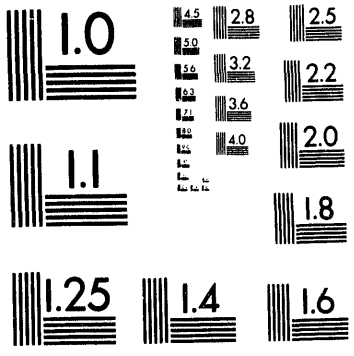

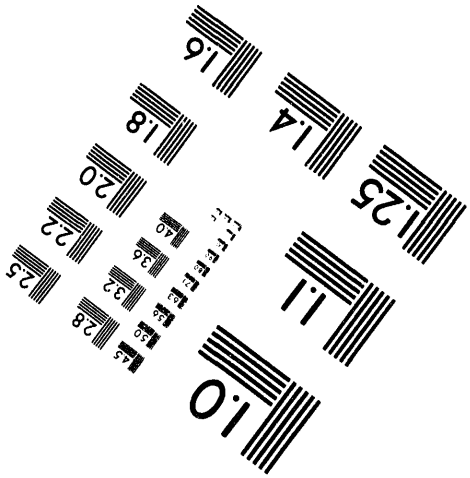

MANUFACTURED TO AIIM STANDARDS
BY APPLIED IMAGE, INC.

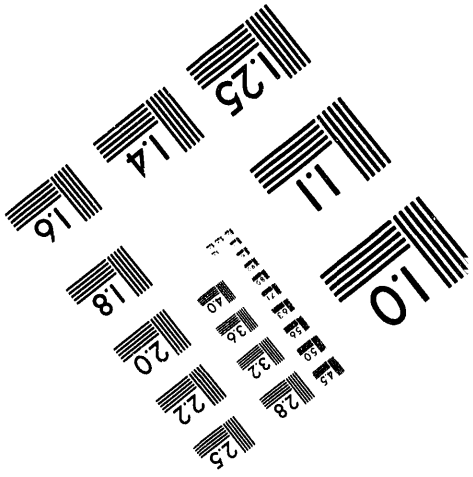

1 of 1

SAND94-0812
TTC 1310
Unlimited Release
Printed April 1994

Distribution
Category UC-820

A COMPARISON OF SPENT FUEL SHIPPING CASK RESPONSE TO 10 CFR 71 NORMAL CONDITIONS AND REALISTIC HOT DAY EXTREMES*

Steven J. Manson and Steven E. Gianoulakis
Transportation Systems Development Department
Sandia National Laboratories**
Albuquerque, NM 87185

Abstract

An examination of the effect of a realistic (though conservative) hot day environment on the thermal transient behavior of spent fuel shipping casks is made. These results are compared to those that develop under the prescribed normal thermal condition of 10 CFR 71. Of specific concern are the characteristics of propagating thermal waves, which are set up by diurnal variations of temperature and insolation in the outdoor environment. In order to arrive at a realistic approximation of these variations on a conservative hot day, actual temperature and insolation measurements have been obtained from the National Climatic Data Center (NCDC) for representatively hot and high heat flux days. Thus, the use of authentic meteorological data ensures the realistic approach sought. Further supporting the desired realism of the modeling effort is the use of realistic cask configurations in which multiple laminations of structural, shielding, and other materials are expected to attenuate the propagating thermal waves. The completed analysis revealed that the majority of wall temperatures, for a wide variety of spent fuel shipping cask configurations, fall well below those predicted by enforcement of the regulatory environmental conditions of 10 CFR 71. It was found that maximum temperatures at the cask surface occasionally lie above temperatures predicted under the prescribed regulatory conditions. However, the temperature differences are small enough that the normal conservative assumptions that are made in the course of typical cask evaluations should correct for any potential violations. The analysis demonstrates that diurnal temperature variations that penetrate the cask wall all have maxima substantially less than the corresponding regulatory solutions. Therefore it is certain that vital cask components and the spent fuel itself will not exceed the temperatures calculated by use of the conditions of 10 CFR 71.

* This work was performed by Sandia National Laboratories for the U.S. Department of Energy under contract DE-AC04-94AL85000

** A U.S. Department of Energy facility.

Acknowledgments

The authors thank W. Lake, M. Brady, and J. Moya for their help and support. The work of Mr. Manson was performed under appointment to the Civilian Radioactive Waste Management Fellowship Program administered by Oak Ridge Institute for Science and Education for the U.S. Department of Energy.

CONTENTS

Figures vi

Tables vii

Acronyms and Abbreviations vii

1.0 INTRODUCTION 1

2.0 AMBIENT CONDITION DATA MODEL 3

2.1 Insolation Data 3
2.2 Temperature Data 5
2.3 Data Transformation 6

3.0 HEAT CONDUCTION MODEL 11

3.1 One-Dimensional Conduction Model 11
3.2 Material Interfaces 13
3.3 Boundary Conditions 15
3.4 Solution Routine 17

4.0 VALIDATION AND BENCHMARKING 21

4.1 Semi-Infinite Constant-Temperature Convection Transient 21
4.2 Semi-Infinite Sinusoidal Convection Transient 23

5.0 RESULTS 27

5.1 Shield Results 30
5.2 Base Results 36
5.3 Geometry Results 37
5.4 Materials Results 38
5.5 Neutron Shield Thickness Results 42
5.6 Convection Results 45

6.0 CONCLUSIONS 47

6.1 Results Summary 47
6.2 Conclusions 47
6.3 Recommendations 48

7.0 REFERENCES 49

APPENDIX A: SOURCE CODE LISTING 51

APPENDIX B: INPUT FILE LISTING 61

FIGURES

		Page
1	Hourly Variation of Insolation Typical Meteorological Year Data	4
2	Hot Day Temperature Variation	5
3	Interpolation of Integral Radiative Heat Flux Versus Time	7
4	Interpolation of Radiative Heat Flux Versus Time	8
5	Interpolation of Temperature Versus Time	8
6	Illustration of the Discretization Scheme, With and Without Insolation Shield	12
7	Illustration of the Interfacial Node	13
8	Flow Chart of Solution Procedure	19
9	A Semi-Infinite Slab Exposed to Convection	21
10	Plot of Numerical and Analytical Solutions of the First Benchmark Problem	22
11	Plot of the L2 Error Norm for the First Benchmark Problem as a Function of Spatial Discretization for Various Time Steps	23
12	Plot of Numerical and Analytical Solutions of the Second Benchmark Problem	24
13	Plot of the L2 Error Norm for the Second Benchmark Problem as a Function of Spatial Discretization for Various Time Steps	25
14	Schematic Drawing of Generic Truck Cask Wall	27
15	Schematic Drawing of Generic Rail Cask Wall	28
16	Truck Cask, Black Shield, Black Surface	30
17	Truck Cask, Grey Shield, Grey Surface	31
18	Truck Cask, Grey Shield, Black Surface	32
19	Truck Cask, Black Shield, Grey Surface	32
20	Rail Cask, Black Shield, Black Surface	33
21	Rail Cask, Grey Shield, Grey Surface	33
22	Rail Cask, Grey Shield, Black Surface	34
23	Rail Cask, Black Shield, Grey Surface	34
24	Truck Cask, No Shield, Grey Surface	35
25	Rail Cask, No Shield, Grey Surface	35
26	Truck Cask, Base Case, Diurnal Variation for Realistic Simulation and Regulatory Conditions	36
27	Rail Cask, Base Case, Diurnal Variation for Realistic Simulation and Regulatory Conditions	36
28	Truck Cask, Base Case, Planar Geometry	37
29	Rail Cask, Base Case, Planar Geometry	38
30	Truck Cask, C/Cu Neutron Shield	39
31	Truck Cask, H_2O Neutron Shield	39
32	Truck Cask, CNF Neutron Shield	40
33	Rail Cask, POLY Neutron Shield	41
34	Rail Cask, H_2O Neutron Shield	41
35	Rail Cask, CNF Neutron Shield	42
36	Truck Cask, Variation of POLY Thickness, Temperature Difference at Solar Shield	43
37	Truck Cask, Variation of POLY Thickness, Temperature Difference at Cask Surface	43
38	Truck Cask, Variation of POLY Thickness, Thickness of POLY Breached by Maximum Profile	44
39	Rail Cask, Variation of CNF Thickness, Temperature Difference at Solar Shield	44
40	Rail Cask, Variation of CNF Thickness, Temperature Difference at Cask Surface	45
41	Truck Cask, Variation of Temperature Difference Versus Convection Coefficient	46
42	Rail Cask, Variation of Temperature Difference Versus Convection Coefficient	46

TABLES

		Page
1	Integrated Radiation Heat Fluence Measurements	4
2	Quantities Evaluated on Each Side of Node i	14
3	Thermal Properties of Materials	29
4	Additional Parameters	29

ACRONYMS AND ABBREVIATIONS

10 CFR 71	Title 10 of the Code of Federal Regulations, Section 71
C/Cu	concrete containing copper fins
CFT	Cosine Fourier Transformation
CNF	concrete without copper fins
DU	depleted uranium
H_2O	water
NCDC	National Climatic Data Center
NRC	U.S. Nuclear Regulatory Commission
Pb	lead
POLY	polypropylene
RC	rail cask
SS	stainless steel
TC	truck cask
TMY	Typical Meteorological Year

1.0 INTRODUCTION

The U.S. Nuclear Regulatory Commission (NRC) has published criteria under which spent fuel shipping containers are to be evaluated in Title 10 of the Code of Federal Regulations, Section 71 (10 CFR 71). Among these requirements is a specification for the normal thermal condition that uses specified bounding conditions based on a generalized hot day in the United States. The regulation specifies an ambient temperature of 100°F, and a daily total insolation of 800 cal/cm^2. As the temperature specified in the regulation is somewhat lower than peak temperatures often reached in the desert southwest region of the country (115°F or more), it has been deemed valuable to compare the effects of an hourly varying, *realistic* temperature cycle to those of the regulation as written. Similarly, the regulation specification for a solar radiation incident on the surface of a cask has a value much less than the peak insolation that may occur at some U.S. latitudes, so a comparison with realistic solar data was also in order. It is expected that the cask materials and their geometrical configurations will have a large impact on the cask response to diurnal variations in ambient temperature and insolation. Thus, a study undertaking a comparison of cask response to realistic and regulatory conditions must examine a number of different cask designs in order to draw conclusions about the general differences between the regulatory and realistic conditions.

Previous studies have shown that the NRC's hot day thermal condition is adequate for predicting the thermal response of the interior regions of large water-cooled shipping casks (Lake, 1980). It has also been shown that the thermal response of the surface regions of casks characterized as simple steel plates are reasonably well represented by using the normal condition of 10 CFR 71 (Brown et al., 1992). Actual cask designs, however, are laminations of several concentric shells with widely varying thermal properties, and hence much more complicated than the steel plates studied by Brown. Furthermore, the studies by Lake and Brown use only simple mathematical functions to represent postulated environmental data. It is thought that by using *actual* hot day data, a more realistic analysis may be performed. Since Brown used a lumped-parameter model, only surface effects were compared between the regulatory model and the postulated conditions. More exact conclusions may be drawn by modeling the spatial propagation of thermal effects through the cask wall, especially in situations involving multiple layers of cask material.

The existing hot day regulatory model consists of a constant environmental temperature of 38°C (311 K, 100°F). This value stands as the 10 CFR 71 hot day ambient temperature despite the fact that peak temperatures in the desert southwest region of the United States are known to occasionally fall in the range of 115° to 120°F in the summer. Peak temperatures in this range occur only for several hours on a hot day, but the existence of such peaks may impact cask thermal performance. However, even on those days when the peak temperature briefly exceeds 115°F, it is certain that the nighttime lows will be substantially less than 100°F. Thus, the average temperature during a 24-hr period on the hottest of days may be close to the CFR prescribed 100°F, and the impact of the temperature peak may be small if the cask is insensitive to short-term thermal transients due to its thermal inertia. It is necessary to support this observation with calculations that demonstrate that cask thermal behavior during peak temperature times in a variable cycle is bounded by, or is approximately represented by, the behavior of a cask subject to the regulation.

Similar concerns exist for the influence of solar radiation incident on a cask surface. The 10 CFR 71 regulation states that a flat, upward-facing surface of a cask will be subject to a total of 800 cal/cm^2 of insolation during each 12-hr daylight period. The regulation, however, does not suggest a temporal distribution for the given heat fluence. This regulation is occasionally applied by subjecting the cask to a constant heat flux of 66.67 cal/cm^2/hr for a 12-hr period, and zero insolation during the remainder of the day. More frequently, a conservative steady-state solution is calculated by assuming that 66.67 cal/cm^2/hr is applied 24 hr a day, despite the fact that this results in twice the required insolation being delivered to the cask. Again, this regulation is not typical of the insolation flux one encounters during an actual day. In fact, solar insolation flux is zero at night, gradually increases during daylight hours, peaks at noon (solar time), and gradually decreases until sunset. However, the total 12-hr insolation fluence of 800 cal/cm^2 (33.5 MJ/m^2), is close to maximum values (around 35 MJ/m^2) typically measured at U.S. latitudes south of 40 deg. Again, the phenomenon of interest is the peaking that occurs above and beyond the two typical implementations of the regulation. This study explicitly determines the extent to which the peak insolation flux affects the components of the cask wall.

The important difference between the regulations as cited and the actual typical meteorological conditions is twofold. First, there is the matter of the peak values of temperature and insolation which both may be, as stated above, potentially larger than the stated regulatory condition. Second, the nature of the diurnal variation of both the temperature and insolation rate suggests that transient thermal behavior not predicted by the regulatory model may occur. These effects compete to a certain extent, and detailed analysis can quantify the overall thermal behavior of transport casks subjected to diurnal variations in ambient conditions.

This report details analyses that address these issues by using a realistic ambient conditions model in conjunction with a one-dimensional transient conduction computer code to determine the thermal response of various cask configurations. Subsequent sections of this report will describe the development of the realistic ambient data model, the formulation of the computational algorithm used to determine cask thermal response, and the benchmarking of that algorithm. Finally, results stemming from the use of the algorithm will be presented and the conclusions that may be drawn from these results will be stated.

2.0 AMBIENT CONDITION DATA MODEL

One goal of this study is the prediction of *realistic* responses to diurnal temperature and insolation variations that would be exhibited by various cask designs. In order to calculate a truly realistic response, it is necessary to use actual observed meteorological data in formulating the boundary surface conditions for the simulation.

Meteorological data are available in a variety of forms from a number of sources. One particular source used in this study has been compiled by the National Climatic Data Center (NCDC). The NCDC has gathered weather data from all over the United States and combined it in a series of records cumulatively referred to as the Typical Meteorological Year (TMY). The TMY is available in subsets according to the region of the United States in which the data were collected. The data for each station location within each region are listed sequentially for each hour during a year's time, and include measurements of the solar radiation, visibility, barometric pressure, ambient temperature, and wind speed.

The data of specific concern for this study are these various solar radiation measurements and the temperature. Solar radiation is measured and reported in five different ways in the TMY data. These solar radiation measurements are evaluated subsequently, and a single measurement technique is chosen as the most applicable, yet conservative means of sampling. The characterization of insolation and temperature together will allow the adequate formulation of a thermal boundary condition for the surface of a cask. The data used for this study will be presented along with the manner in which they were obtained.

2.1 Insolation Data

The NCDC TMY insolation data are provided by several different measurements:

1. Direct Normal Radiation
2. Global Radiation on a Tilted Surface
3. Observed Global Radiation on a Horizontal Surface
4. Corrected Global Radiation on a Horizontal Surface
5. Standard-Year Corrected Global Radiation on a Horizontal Surface

Each of these measurements is provided for each location in the region. The meanings of the various measurements are described below.

Direct normal radiation is a measurement of the collimated insolation that intersects an area normal to the direction of the flux. Since the normal surface is made to track the sun during the day, the net integrated heat flux is higher than the corresponding measurement for a fixed surface. However, since the radiation is collimated, the peak flux is usually much less than the corresponding global measurement.

Global radiation refers to all incident solar radiation on a surface, including that component which is incident upon the surface due to scattering in the atmosphere. This component is eliminated during the collimation process of the direct normal measurement. Global insolation measurements are recorded for a horizontal surface and a stationary tilted surface. Total integral flux measurements are typically higher for the tilted case in regions removed from the equator because the sun's rays are typically not perpendicular to the horizontal plane.

Two engineered corrections are applied to the raw data to obtain the corrected global horizontal measurements. In the first case, the data from the direct measurement are corrected for experimental error. This correction usually results in a smaller value of incident radiative flux for particularly high flux days, which are of most interest here. Secondly, the observed data are manipulated to approximate the so called "typical year" by an averaging technique (TMY User's Manual, 1981).

The TMY data available for this study cover Regions 3 and 6 of the United States. These regions are comprised of the Central Plains and Lower Mississippi Valley, and Texas and New Mexico, respectively. While these regions are not the hottest in the United States, the quantity of immediate interest is insolation, and these data are a representative sample of the latitudes ranging from 28 to 40 deg north.

This sample may be called representative because the insolation data for the high radiation day are predominantly a function of latitude, and not a function of weather patterns, although some variation due to average cloud cover may exist. The variations due to cloud cover may be removed by searching for the maximum insolation day, which will, quite expectedly, fall on a cloudless day.

All data for Region 3 were searched to locate each day in which the integrated radiation flux (total fluence) was a maximum for one of the five recorded measurements, as previously described. The five maxima were comprised of only three different measurement days, all occurring in Dodge City, Kansas. The TMY data for Region 6 only included the standard year measurement, but were also searched for the high fluence day. When this day's data were compared to the high fluence day for the standard year data of Region 3, it was found that the Region 3 insolation was much greater than that for any Region 6 location. The integrated radiation heat flux values for the three maximum days are compiled in Table 1.

Table 1. Integrated Radiation Heat Fluence Measurements
(Fluence in kJ/m^2, Maximum Values Denoted by *)

Location	Date	Direct Normal	Global Tilted	Horizontal Observed	Horizontal Corrected	Standard Year
Dodge City	25-June	42129*	31155	30600	32575	31343
Dodge City	29-May	33791	34958*	33895	31470	34587*
Dodge City	3-July	39677	34463	34559*	34096*	34559

A plot of the hourly variation of each of the maximum data sets appears in Figure 1 as a function of the solar time (not the clock time) at the geographic location. The area under the curve (the total daily insolation) is a maximum for the direct normal data. Furthermore, the peak flux is the most depressed for that set as well. The peak flux (as well as integral flux) of the tilted case is highest among the stationary global measurements.

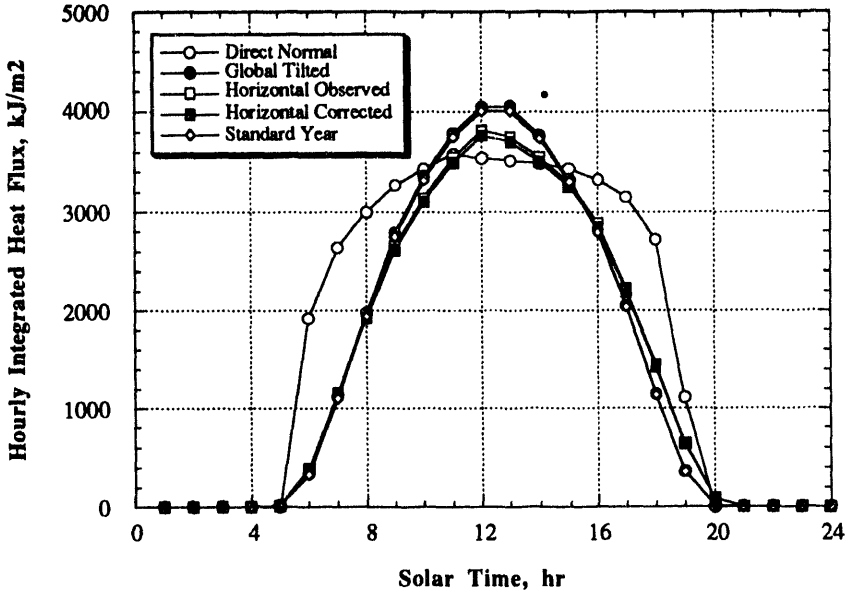

Figure 1. Hourly Variation of Isolation Typical Meteorological Year Data

Having selected the maximum insolation days in each of the measurement categories, it is now necessary to determine which data set is most applicable for use in modeling a shipping cask exposed to a hot day environment. It is appropriate to begin by eliminating the direct normal case due to the fact that it is necessary for the surface to be in constant motion, tracking the sun, in order to maintain the normal orientation relative to the sun's rays. Furthermore, it is apparent from the plot in Figure 1 that the peak values for the standard year and global tilted data lie well above those of horizontal observed and horizontal corrected data. In the interest of maintaining a reasonable though conservative model, the maximum of these the global tilted data set is chosen for this study. Whereas the standard year data are recommended by the NCDC as the best available data, the tilted data appear to lie close to these values and yet be maximum. Strengthening the qualification of this data set is the fact that most cask designs are cylindrical; thus, some surface of the cask may be tilted at all times in the same manner as the apparatus that produced the global tilted measurements.

2.2 Temperature Data

Unlike the insolation data that vary predominantly as a function of latitude, temperature is a more complex phenomenon, being subject to the dominant weather patterns of the location. However, it is known that the most consistently extreme hot temperatures in the contiguous United States are found in the Desert Southwest, which includes sections of Arizona, New Mexico, California, Utah, and Nevada. Yuma, Arizona is typical of the hottest inhabited locations in the United States (Gringorten et al., 1985).

Thus, the TMY data for Yuma were obtained from the NCDC in order to determine a reasonable hourly variation pattern for temperature on the hottest day of a typical year. What is not known, however, is the hourly variation of temperature on the hottest day over a period spanning many years. The most extreme temperature in recorded U.S. history is known to be 57°C (330 K, 135°F). Thus, if desired, the temperature profile for the hot standard day in Yuma can be augmented to conform to the recorded maximum.

The data for the TMY day (and a day before and after), which has both the hottest average temperature for the 24-hr period and contains the hottest hour in the TMY for Yuma, are plotted in Figure 2 as a function of the local solar time. The most surprising feature of the data in Figure 2 is the lack of smoothness. Furthermore, it is noted that the hottest 24-hr period is that from 6 A.M., July 10, to 6 A.M., July 11, not the period from midnight to midnight. The difference in the average temperatures for the two time periods is minimal; however, choosing to model the period from 6 A.M. does make the diurnal temperature cycle somewhat smoother than the periodic cycle produced from midnight to midnight.

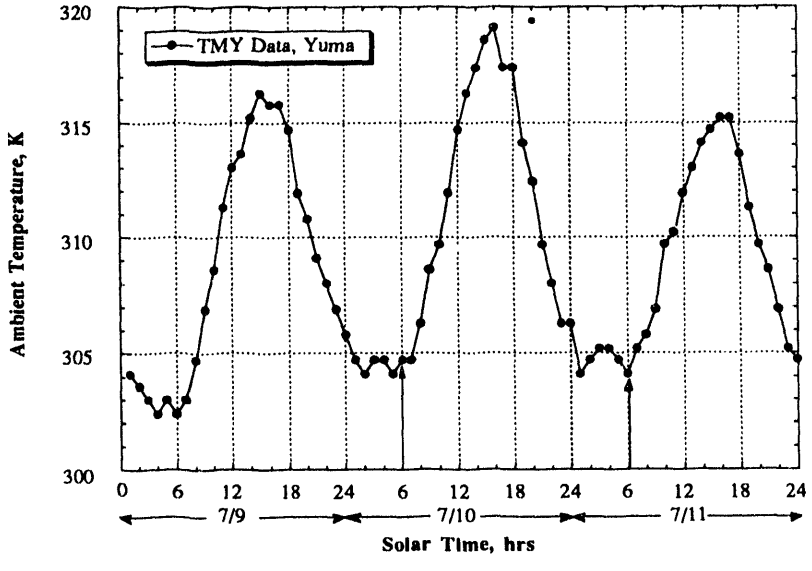

Figure 2. Hot Day Temperature Variation

2.3 Data Transformation

The measurements provided in the TMY data sets are recorded in hourly increments. However, a *realistic* thermal simulation that uses these data will have a time step smaller than 1 hr. It becomes necessary to interpolate the data in some manner in order to provide insolation or temperature boundary conditions at any instant over the course of a day.

There is an abundance of interpolation routines that may prove useful for the present application. However, due to the general shape of the data, the Cosine Fourier Transformation (CFT) was chosen for use in evaluating the data. The CFT is particularly suitable due to its inherent ability to evaluate the derivative of a function once the CFT of the function is known. This ability is helpful when evaluating the insolation data, since the TMY data provide measurements of the insolation fluence during each hour previous to the recording of the measurement, which is effectively the integral of the radiation flux. Thus the insolation rate may be recovered from the data by taking the derivative of the fluence value. The differentiation process will subsequently be described in greater detail. The CFT process is explained below.

Given any finite, discrete set of data, s_n (n = 1, 2, 3,...,N) taken at evenly spaced intervals, the CFT may be calculated by first extending the data in the form of an *even* periodic series. We now have s_n (n = 1, 2, 3, ..., 2N), where:

$$s_n = \begin{cases} \text{data}, & 1 < n < N \\ s_{2N-n}, & N < n < 2N \end{cases} \tag{1}$$

The coefficients of the cosine transformation, c_m (m = 1, 2, 3, ..., 2N), are then determined as (IMSL Math Library, 1987):

$$c_m = s_1 + s_{2N}(-1)^{m-1} + 2\sum_{n=2}^{2N-1} s_n \cos\left[\frac{(m-1)(n-1)\pi}{2N-1}\right] \tag{2}$$

This formulation of the CFT has the advantage of being its own inverse. That is, once the coefficients are known, the original data can be recovered by using the same function above and subsequently dividing the result by (4N – 2). In addition, the inverse transform can be used to interpolate the function. Realizing that if each of s_m observations are equally spaced in time, τ, with $m = 1$ corresponding to $\tau = 0$, then:

$$\tau = \frac{m-1}{2N-1} \tag{3}$$

This expression can be substituted into the inverse transform directly, so for any time τ the corresponding value of s, the continuous function, is:

$$s = \frac{1}{4N-2}\left(c_1 + c_{2N} + 2\sum_{n=2}^{2N-1} c_n \cos[\tau(n-1)\pi]\right) \tag{4}$$

Returning to consider the insolation data explicitly, it is now noted that the form of the data is actually a period integral. Each measurement, as opposed to being an instantaneous measurement of heat flux at the time of the measurement, is instead the total incident radiation energy during the previous hour. Therefore, the most accurate interpretation of this data is as a strict integral; each measurement should be added to the previous ones to get a value of the total insolation up to that point during the day. Performing this operation, and then the CFT, we are left with an interpolation of the integral heat flux. This interpretation of the insolation data is demonstrated explicitly in Figure 3.

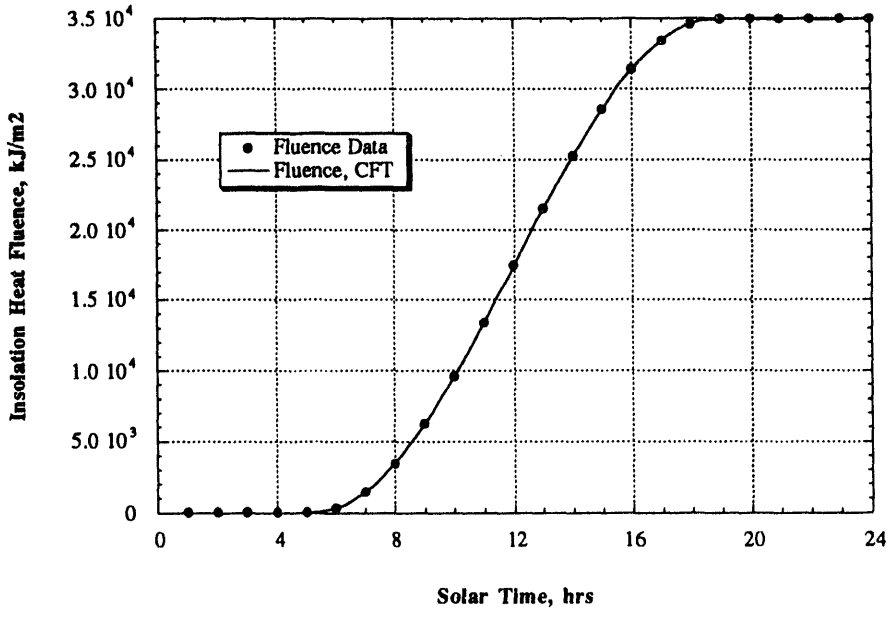

Figure 3. Interpolation of Integral Radiative Heat Flux Versus Time

However, the heat conduction equation will require a statement of the actual insolation rate, again at any given instant. This can be remedied by taking the derivative of the integral function. This operation can be performed during the process of inverting the coefficients of the transformation. The derivative of the function can be found by calculating:

$$s' = \frac{1}{4N-2}\left(-2\pi \sum_{n=2}^{2N-1} c_n(n-1)\sin[\tau(n-1)\pi]\right) \tag{5}$$

for each heat flux required. Figure 4 shows the derivative transformation alongside the hourly step-wise integrated data. The phase shift present in Figure 4 is due to the lack of equivalence of the hourly integral heating data and the real time derivative of the fluence. The extra line shown in Figure 4 was calculated by performing the continuous hourly integration of the CFT flux. Each point along this curve was calculated by integrating the flux over the previous 60 minutes. This calculation demonstrates explicitly that the phase shift is entirely due to the hourly integration procedure that is inherent in the TMY data. The small error in the hourly integrated flux for the CFT as compared to the data demonstrates that the correlation of the interpolating function as derived is good.

Since the temperatures are recorded as instantaneous values at each hour, the simple transformation/ inversion routine shown initially will work without the need for differentiation. Figure 5 shows the correlation of the temperature data and their CFT interpolation. The data from midnight to 6 A.M. come from the TMY date July 11, the remainder from July 10. Thus, the nighttime data have been rotated around to the beginning in this plot. This is not out of the ordinary as the data are being interpreted as a periodic function with respect to time. Additionally, the CFT function (which is graphed with the original TMY data) has been smoothed to eliminate the small order oscillations present in the data. The peak temperature has been preserved, as well as the general form of the diurnal variation; however, smaller oscillations that do not contribute to the general, overall diurnal behavior are expunged. Had the small oscillations been retained, physically unrealistic "wiggles" in the CFT interpolation would have resulted.

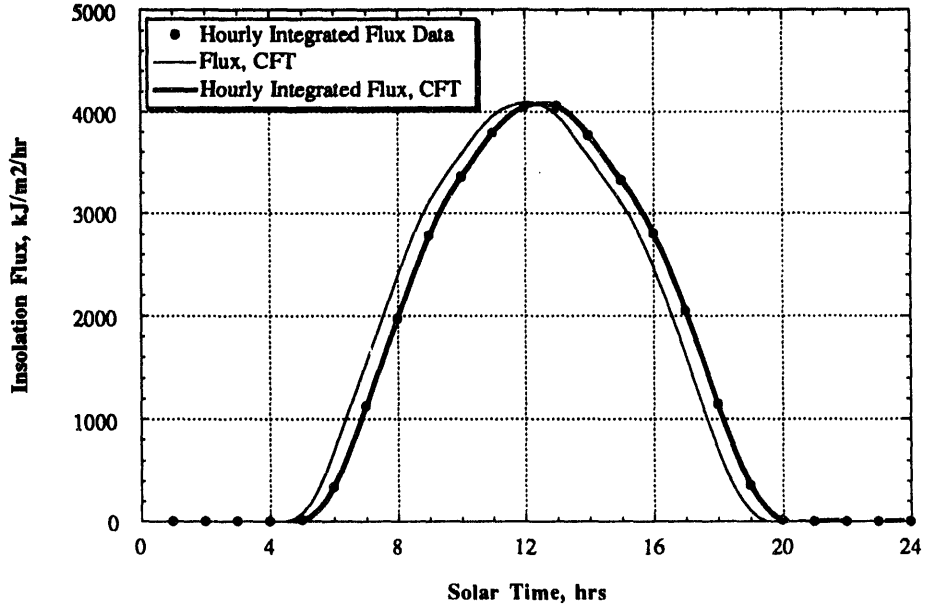

Figure 4. Interpolation of Radiative Heat Flux Versus Time

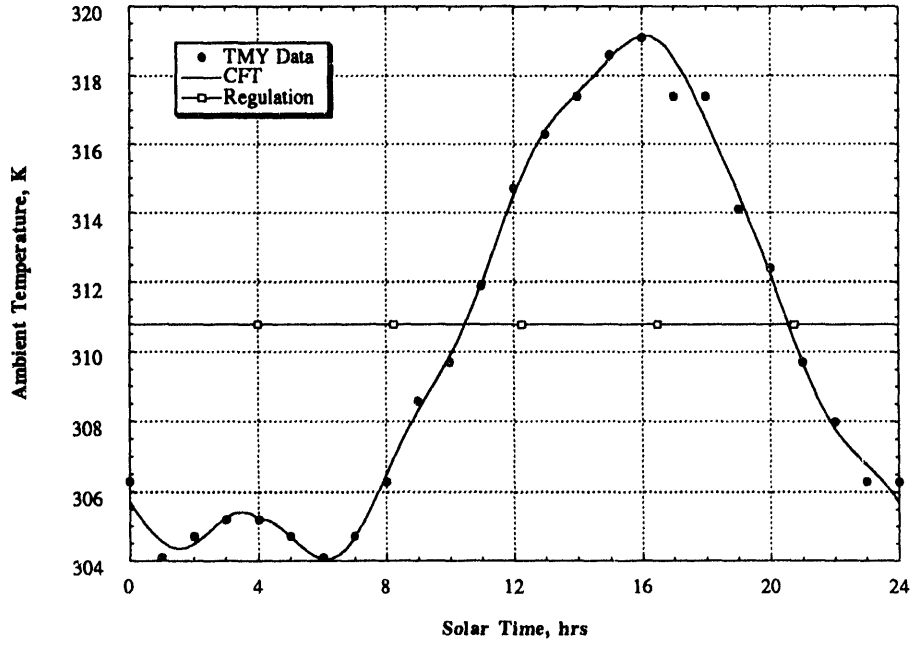

Figure 5. Interpolation of Temperature Versus Time

The smoothing was performed by canceling 20 (out of 48) of the higher order terms of the CFT by setting their coefficients equal to zero. These coefficients correspond to cosine waves with the smallest periods and are most responsible for the extremely localized "wiggling."

3.0 HEAT CONDUCTION MODEL

To determine the penetrative effects of the diurnal variation of temperature and insolation, and thereby the maximum temperature profile through the cask wall, it was necessary to formulate an appropriate transient heat conduction model. The subject model accurately represents the geometry of interest and yet is only one-dimensional. Since it is necessary that the model correctly represent transient events taking place over the course of periodic diurnal variations, the associated computational method was formulated to be time-accurate. Finally, to facilitate the modeling of a large variety of cask configurations, the model had to be capable of incorporating any number of laminations of any user-specified material and thickness into the geometrical formulation. In the derived formulation, each lamination may be specified as having any thickness and may be discretized into any number of nodes to capture the thermal gradient across the layer.

While the computational method is one-dimensional, the code has been written in two implementations: one in planar (Cartesian) geometry, and the other in cylindrical (radial) geometry. This allows the code to have added flexibility in modeling: the side walls of most casks are cylindrical in shape while the ends are flat. This difference in configuration may have some importance in the propagation of the diurnal ambient conditions.

The exterior boundary condition in the computational model is such that the temperature and insolation data interpolations described in the previous section may be implemented in a straightforward fashion. The exterior of the cask may be analyzed in two different configurations, either with or without taking into account the presence of an insolation shield or personnel barrier. The internal boundary condition may be set to model any level of internal heat generation. This is accomplished by setting a constant level of heat flux at the interior wall.

3.1 One-Dimensional Conduction Model

The general one-dimensional transient heat conduction equation in Cartesian coordinates is given as (Gebhart, 1993):

$$\frac{\partial}{\partial x}\left(k_x \frac{\partial t}{\partial x}\right) + q''' = \rho c_p \frac{\partial t}{\partial \tau} \tag{6}$$

In this notation, t is temperature, τ is time, x is the spatial coordinate, k_x is the thermal conductivity as a function of x, q''' is the generation term, ρ is the material density, and c_p is the material specific heat.

For regions away from material interfaces, where k_x, ρ, and c_p can be treated as constants (we will return later to treat specifically those interface regions) and with no generation term, the expression may be simplified (deleting the subscript from k as it is now independent of position):

$$k \nabla^2 t = \rho c_p \frac{\partial t}{\partial \tau} \tag{7}$$

Making use of the thermal diffusivity, $\alpha = k/(\rho c_p)$:

$$\nabla^2 t = \frac{1}{\alpha} \frac{\partial t}{\partial \tau} \tag{8}$$

The Laplacian, $\nabla^2 t$, has alternate implementations in rectangular and cylindrical coordinates (in the radial direction, r):

$$\nabla^2 t = \frac{\partial^2 t}{\partial x^2}, \text{ and } \nabla^2 t = \frac{\partial^2 t}{\partial r^2} + \frac{1}{r}\frac{\partial t}{\partial r} \tag{9}$$

respectively. For the cylindrical case the heat equation becomes:

$$\frac{\partial^2 t}{\partial r^2} + \frac{1}{r}\frac{\partial t}{\partial r} = \frac{1}{\alpha}\frac{\partial t}{\partial \tau} \tag{10}$$

Note that the rectangular form may be recovered by setting the term $1/r$ equal to zero for all space and replacing r with x.

Using the *interior* node finite difference scheme represented in Figure 6, spatial discretization of this equation using central differencing yields:

$$\frac{t_{i+1} - 2t_i + t_{i-1}}{\Delta r^2} + \frac{1}{r_i}\frac{t_{i-1} - t_{i+1}}{2\Delta r} = \frac{1}{\alpha}\frac{\partial t}{\partial \tau} \tag{11}$$

Temporal discretization is derived by use of the implicit method, giving:

$$\frac{t_{i+1} - 2t_i + t_{i-1}}{\Delta r^2} + \frac{1}{r_i}\frac{t_{i-1} - t_{i+1}}{2\Delta r} = \frac{1}{\alpha}\frac{t_i - t_i^{old}}{\Delta \tau} \tag{12}$$

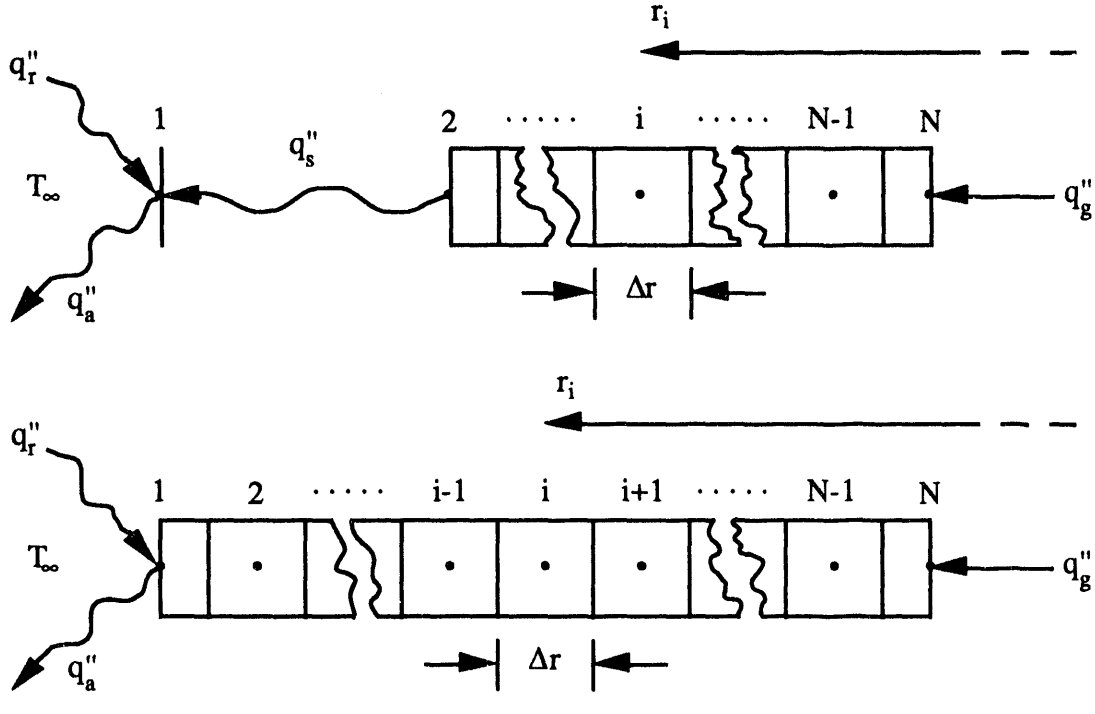

Figure 6. Illustration of the Discretization Scheme, With (Top) and Without Insolation Shield (Bottom)

This expression can be rewritten for use in a tridiagonal matrix solution algorithm. The form is then:

$$\left(\frac{\Delta r}{2r_i}-1\right)t_{i+1}+\left(\frac{\Delta r^2}{\alpha\Delta\tau}+2\right)t_i+\left(\frac{-\Delta r}{2r_i}-1\right)t_{i-1}=\frac{\Delta r^2}{\alpha\Delta\tau}t_i^{old} \tag{13}$$

The tridiagonal matrix solution algorithm is well documented (Press et al., 1989) and can be implemented successively for transient solutions of the above representation of the conduction equation, on the interior domain of any layer. The remaining equations required to specify the boundary conditions and to describe conduction at the material interfaces will also be implemented in a form compatible with the tridiagonal solution routine. These equations are developed subsequently.

3.2 Material Interfaces

Simulation of the heat conduction process at an interface between two adjacent layers can be performed via a reformulated conduction equation that takes into account the change in material properties at the discontinuity. Beginning with the general one-dimensional transient conduction equation in cylindrical coordinates:

$$\frac{1}{r}\frac{\partial}{\partial r}\left(r\,k_r\frac{\partial t}{\partial r}\right)=\rho c_p\frac{\partial t}{\partial \tau} \tag{14}$$

We have again eliminated the volumetric source term, q''', thus it remains to evaluate the left-hand side of the equation above. Figure 7 depicts the interface between two materials, generically referred to as materials *n* and *n+1*. Considering a geometry of the form shown in Figure 7, with the node *i* located on the actual interface, the term inside the parentheses in Equation 14 may be evaluated at the eastern and western boundaries of the volume at node *i*.

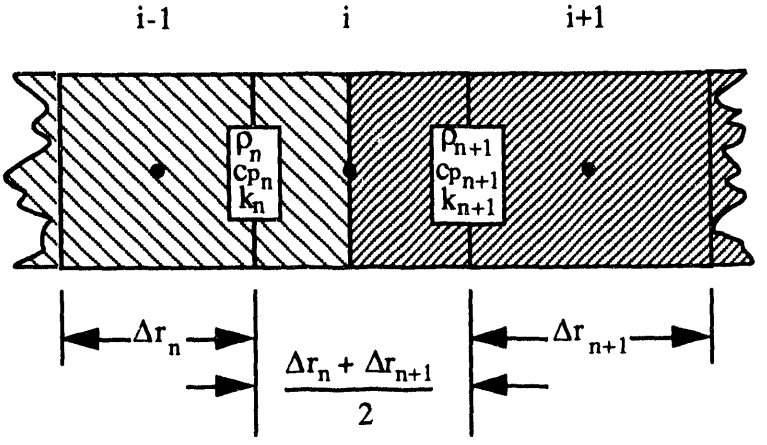

Figure 7. Illustration of the Interfacial Node

An explicit statement of the terms present inside the derivative, and evaluated on the boundaries of the interfacial volume are given in Table 2.

Combining the terms to calculate the derivative at the cell center results in:

$$\frac{1}{r_i}\frac{2}{\Delta r_n+\Delta r_{n+1}}\left\{\left[\left(r_i-\frac{\Delta r_{n+1}}{2}\right)k_{n+1}\frac{t_{i+1}-t_i}{\Delta r_{n+1}}\right]-\left[\left(r_i+\frac{\Delta r_n}{2}\right)k_n\frac{t_i-t_{i-1}}{\Delta r_n}\right]\right\}=\rho c_p\frac{\partial t}{\partial \tau} \tag{15}$$

Table 2. Quantities Evaluated on Each Side of Node i

	West	East
$\frac{\partial t}{\partial r}$	$\frac{t_i - t_{i-1}}{\Delta r_n}$	$\frac{t_{i+1} - t_i}{\Delta r_{n+1}}$
k	k_n	k_{n+1}
r	$r_i + \frac{\Delta r_n}{2}$	$r_i - \frac{\Delta r_{n+1}}{2}$

Next, it is necessary to evaluate the density, ρ, and the specific heat, c_p, for the interfacial volume. Since the density is a volumetric property, the density of each material at the interfacial element is proportional to the volume of the material there, which in turn may be set equal to the differential length in each direction. Thus:

$$\rho_i = \left(\frac{\rho_n \Delta r_n + \rho_{n+1} \Delta r_{n+1}}{\Delta r_n + \Delta r_{n+1}} \right) \tag{16}$$

Specific heat, however, is a mass-intensive property and must be evaluated based on the relative amount of mass of each material present in the volume. Thus, each component of specific heat is proportional to density multiplied by the differential length, and therefore:

$$c_{pi} = \left(\frac{c_{pn} \rho_n \Delta r_n + c_{pn+1} \rho_{n+1} \Delta r_{n+1}}{\rho_n \Delta r_n + \rho_{n+1} \Delta r_{n+1}} \right) \tag{17}$$

Substituting these expressions into the transient conduction equation for the interfacial node and simplifying, yields:

$$\frac{1}{\Delta r_n + \Delta r_{n+1}} \left\{ \left[\left(\frac{2}{\Delta r_{n+1}} - \frac{1}{r_i} \right) k_{n+1} (t_{i+1} - t_i) \right] - \left[\left(\frac{2}{\Delta r_n} + \frac{1}{r_i} \right) k_n (t_i - t_{i-1}) \right] \right\}$$
$$= \left(\frac{c_{pn} \rho_n \Delta r_n + c_{pn+1} \rho_{n+1} \Delta r_{n+1}}{\Delta r_n + \Delta r_{n+1}} \right) \frac{\partial t}{\partial \tau}$$

The previous equation can be easily written in implicit form for use in the tridiagonal matrix solver which is, in turn, used to calculate the time-dependent temperature variation over the entire thickness of the cask wall. The form of this equation is:

$$\frac{k_{n+1}}{\Delta r_n + \Delta r_{n+1}}\left(\frac{1}{r_i} - \frac{2}{\Delta r_{n+1}}\right) t_{i+1} +$$

$$\left[\frac{k_{n+1}}{\Delta r_n+\Delta r_{n+1}}\left(\frac{2}{\Delta r_{n+1}} - \frac{1}{r_i}\right) + \frac{k_n}{\Delta r_n+\Delta r_{n+1}}\left(\frac{2}{\Delta r_n} + \frac{1}{r_i}\right) + \left(\frac{c_{pn}\,\rho_n\,\Delta r_n + c_{pn+1}\,\rho_{n+1}\,\Delta r_{n+1}}{\Delta\tau\left(\Delta r_n + \Delta r_{n+1}\right)}\right)\right] t_i + \tag{18}$$

$$\frac{-k_n}{\Delta r_n + \Delta r_{n+1}}\left(\frac{2}{\Delta r_n} + \frac{1}{r_i}\right) t_{i-1} = \left(\frac{c_{pn}\,\rho_n\,\Delta r_n + c_{pn+1}\,\rho_{n+1}\,\Delta r_{n+1}}{\Delta\tau\left(\Delta r_n + \Delta r_{n+1}\right)}\right) t_i^{old}$$

Again, it is relevant to point out that in the case of a rectangular, planar system, the above equation can be used by setting $1/r_i = 0$.

3.3 Boundary Conditions

As the subject model is one-dimensional and time-accurate, it is necessary to define two boundary conditions in addition to an initial condition. Since the data of interest are calculated only after a truly periodic transient cycle is achieved, the initial condition is arbitrary. It remains, then, to illustrate the formulations of the interior and exterior boundary conditions.

Inside the cask is spent nuclear fuel that generates heat at a known rate. The actual generation rate is variable and depends on the specific composition of the fuel, the amount of time and the power at which it was irradiated, and the amount of time since the fuel was removed from the reactor. In general, the heat generation rate of any specific fuel bundle will be calculable based on the above known quantities. When the heat generation rate of each bundle is known, the total interior heat rate can be determined by summation. Finally, the quantity of interest to the calculation of transient temperature profile is just the heat flux at the interior surface of the cask wall, q_g''. This quantity is calculated by simply dividing the total heat generation rate by the total surface area of the cask interior.

Once the interior heat flux has been calculated, it may be implemented in the computational algorithm in a straightforward manner. Gebhart gives the following form of a general surface boundary condition, with the node at the surface (Gebhart, 1993):

$$\frac{k}{\Delta x}(t_1 - t_s) + \left(\frac{q'''\,\Delta x}{2}\right) + q_s'' + h\left(t_\infty - t_s\right) = \frac{\rho\,c_p\,\Delta x}{2\,\Delta\tau}\left(t_s - t_s^{old}\right) \tag{19}$$

In Gebhart's notation, the subscript s denotes the quantity at the surface node, h is the convection coefficient, t_∞ is the ambient temperature, t_1 is the temperature of the node adjacent to the surface, and the surface heat flux is q_s''. The unnecessary terms may be eliminated and the nomenclature can be made to resemble (reverting to the radial coodinate, r) the conventions used previously to give, in cylindrical coordinates:

$$\frac{k}{2}(t_{N-1} - t_N)\left(\frac{2}{\Delta r} + \frac{1}{r_N}\right) + q_g'' = \frac{\rho\,c_p\,\Delta r^2}{8\Delta\tau}\left(t_N - t_N^{old}\right)\left(\frac{4}{\Delta r} + \frac{1}{r_N}\right) \tag{20}$$

Here we recognize the convention established in Figure 6, where the interior surface node is node N. Again, by setting $(1/r_N = 0)$ the equation for a planar wall may be recovered.

The external surface of the spent fuel shipping cask is exposed to an ambient temperature, t_∞, that results in convective heat transfer proportional to the convection coefficient h. Additional energy is transferred to the environment by thermal radiation, q_a''. Furthermore, the surface also absorbs incident solar radiation, q_r'', that along with t_∞ will be obtained from the data interpolations formulated in the previous section.

To develop the numerical form of the exterior surface boundary condition, the general expression is again used. This equation is converted to cylindrical coordinates, and the unnecessary term is eliminated. The equation becomes:

$$\frac{k}{2}(t_2 - t_1)\left(\frac{2}{\Delta r} - \frac{1}{r_1}\right) + q_r'' - q_a'' + h(t_\infty - t_1) = \frac{\rho c_p \Delta r^2}{8\Delta\tau}(t_1 - t_1^{old})\left(\frac{4}{\Delta r} - \frac{1}{r_1}\right) \quad (21)$$

Node *1* is on the exterior surface and node *2* is adjacent. The form of this equation is consistent with Figure 6 and ($1/r_1 = 0$) gives the Cartesian formulation. While the convection and solar radiation terms are defined by the data interpolations, the ambient thermal radiation term, q_a'' is not, and thus needs further specification.

The net thermal radiation, q_{ij}, exchanged between two grey surfaces, i and j, is given as (Incropera and DeWitt, 1981):

$$q_{ij} = A_i F_{ij} \sigma\varepsilon \left(t_i^4 - t_j^4\right) \quad (22)$$

where A_i is the area of surface i, F_{ij} is the view factor from i to j, ε is the surface emissivity and σ is the Stefan-Boltzmann constant. Since the view factor from the cask surface to the environment is 1.0, and since we require a statement of the heat flux at i, the equation can be divided by area, A_i, and simplified to yield:

$$q''_i = \sigma\varepsilon \left(t_i^4 - t_j^4\right) \quad (23)$$

Since the equation requires the fourth power of the local temperature t_j, this term is nonlinear and will not fit into the tridiagonal matrix solution algorithm. Fortunately, this term may be linearized by taking advantage of an explicit approximation of the local temperature, as follows. The radiation heat flux equation can be rewritten by decomposition of the difference squares:

$$q''_i = \sigma\varepsilon \left(t_i^2 - t_j^2\right)\left(t_i^2 + t_j^2\right) \quad (24)$$

which may be further broken down to yield:

$$q''_i = \sigma\varepsilon (t_i - t_j)(t_i + t_j)\left(t_i^2 + t_j^2\right) \quad (25)$$

Using the explicit temperature for node i in the summation terms and the implicit value in the difference term, we arrive at the linearized form:

$$q''_i = \sigma\varepsilon \left(t_i^{new} - t_j\right)\left(t_i^{old} + t_j\right)\left(t_i^{old2} + t_j^2\right) \quad (26)$$

Use of this semi-implicit method in a transient simulation results in some additional error. Sensitivity analyses have shown that if the surface temperature changes less than 5 K in each time step, the error is less than 2% for the range of temperatures of interest in this application. Furthermore, if temperature changes are reduced to 0.1 K per time step, a much more realistic value, the error drops to approximately 0.05%, which is within the uncertainty of the temperature data reported in the TMY.

When the insolation shield is a desired constituent of the analysis, an additional boundary condition must be formulated. Additionally, the equation already derived for the surface of the cask must be modified. The surface equation was given previously as:

$$\frac{k}{2}(t_2 - t_1)\left(\frac{2}{\Delta r} - \frac{1}{r_1}\right) + q_r'' - q_a'' + h(t_\infty - t_1) = \frac{\rho c_p \Delta r^2}{8\Delta\tau}(t_1 - t_1^{old})\left(\frac{4}{\Delta r} - \frac{1}{r_1}\right) \quad (27)$$

Now the convection term is eliminated, as is the insolation term, and the thermal radiation term, q_S'', now interacts with the insolation shield instead of the environment. This results in a new form:

$$\frac{k}{2}(t_3 - t_2)\left(\frac{2}{\Delta r} - \frac{1}{r_2}\right) + q_s'' = \frac{\rho c_p \Delta r^2}{8\Delta\tau}\left(t_2 - t_2^{old}\right)\left(\frac{4}{\Delta r} - \frac{1}{r_2}\right) \tag{28}$$

In this equation the cask surface is now node number *2*, and node *3* (see Figure 6) is its nearest neighbor on the interior of the cask wall.

The original form of the surface equation may be used as a starting point for the derivation of the shield equation:

$$\frac{k}{2}(t_2 - t_1)\left(\frac{2}{\Delta r} - \frac{1}{r_1}\right) + q_r'' - q_a'' + h\left(t_\infty - t_1\right) = \frac{\rho c_p \Delta r^2}{8\Delta\tau}\left(t_1 - t_1^{old}\right)\left(\frac{4}{\Delta r} - \frac{1}{r_1}\right) \tag{29}$$

Now node *1* refers to the shield, and node 2 to the cask surface. It is necessary to add a radiation flux term to account for the thermal radiation between the shield and cask surface while eliminating the terms representing conduction and transient storage, as the shield is taken to possess negligible thermal mass ($c_p = 0$). This yields:

$$q_r'' - q_a'' - q_s'' + h\left(t_\infty - t_1\right) = 0 \tag{30}$$

The ambient and surface radiation heat fluxes, q_a'' and q_S'', are easily approximated by the radiant term linearization as presented previously, with the same attendant error. The surface radiation heat flux, q_a'', is defined for two infinite parallel grey surfaces as (Incropera and DeWitt, 1981):

$$q''_{i,j} = \frac{\sigma\left(t_i^4 - t_j^4\right)}{\frac{1}{\varepsilon_i} + \frac{1}{\varepsilon_j} - 1} \tag{31}$$

This approximation is sufficient to describe the interaction of the shield and the cask surface, as the shield should have very little radiation interaction with itself. The expression when converted to the linearized form becomes:

$$q''_{i,j} = \frac{\sigma\left(t_i^{new} - t_j^{new}\right)\left(t_i^{old} + t_j^{old}\right)\left(t_i^{old2} + t_j^{old2}\right)}{\frac{1}{\varepsilon_i} + \frac{1}{\varepsilon_j} - 1} \tag{32}$$

This can be readily adapted into the requisite form for the tridiagonal matrix solver.

Together, the equations for the interior nodes, interfacial nodes, and boundary nodes constitute a complete set of governing equations. When these equations are solved simultaneously over time, they yield the transient temperature distribution throughout the cask wall.

3.4 Solution Routine

The previous portion of this section was dedicated to the derivation of the equations which will be used to solve the one-dimensional transient heat conduction model in an implicit form. The present discussion will address the implementation of these equations in a computer program designed to determine the temperature variations, both spatial and temporal, in a multi-layer cask wall.

Figure 8 shows a flow chart depicting the macroscopic algorithm for solution of the given simulation. In the preprocessing phase, all array variables are initialized and the input data are read from a file. Input data consist of specifications of the initial condition, the problem geometry, parameters that specify certain options to be used in the solution procedure, the thermal properties of the materials of which the cask is composed, and finally, the data necessary to calculate the interpolations of the ambient temperature and insolation. During the initialization phase, the CFT coefficients are calculated from the temperature and insolation input data. Following the initialization step, the time step is incremented and calculation of the conduction solution at the first time step begins. The solution phase begins by calculating the boundary condition parameters from their CFT coefficients, for the current time. With these parameters known, the construction of the solution matrices begins. The tridiagonal matrix coefficients are then calculated for each node in the wall. This set of linear equations is then solved by decomposition and back substitution (Press et al., 1989). Once the matrix has been solved, it is necessary to store the current solution. Furthermore, if the current time in the simulation happens to be midnight, the current solution is additionally stored in a separate array for later use in determining convergence. If the current time is not midnight, the process returns to the point that the time step was incremented and the process repeats, using the same 24-hr diurnal cycle as the previous day.

After each day's worth of transient calculations, the entire temperature profile in the wall at midnight is compared to that profile that occurred 24 hr earlier. This allows the determination of whether the transient solution has become truly periodic. Periodicity will always develop due to the 24-hr periodic cycle imposed by the boundary conditions. When the maximum variation (from midnight to midnight) in temperature at every node is less than a specified convergence criterion, a steady periodic solution is said to have been reached. When this occurs, the code post processes the solution data. If steady periodicity has not yet been achieved, the code returns to increment the time step again and to calculate the variation for the next whole day.

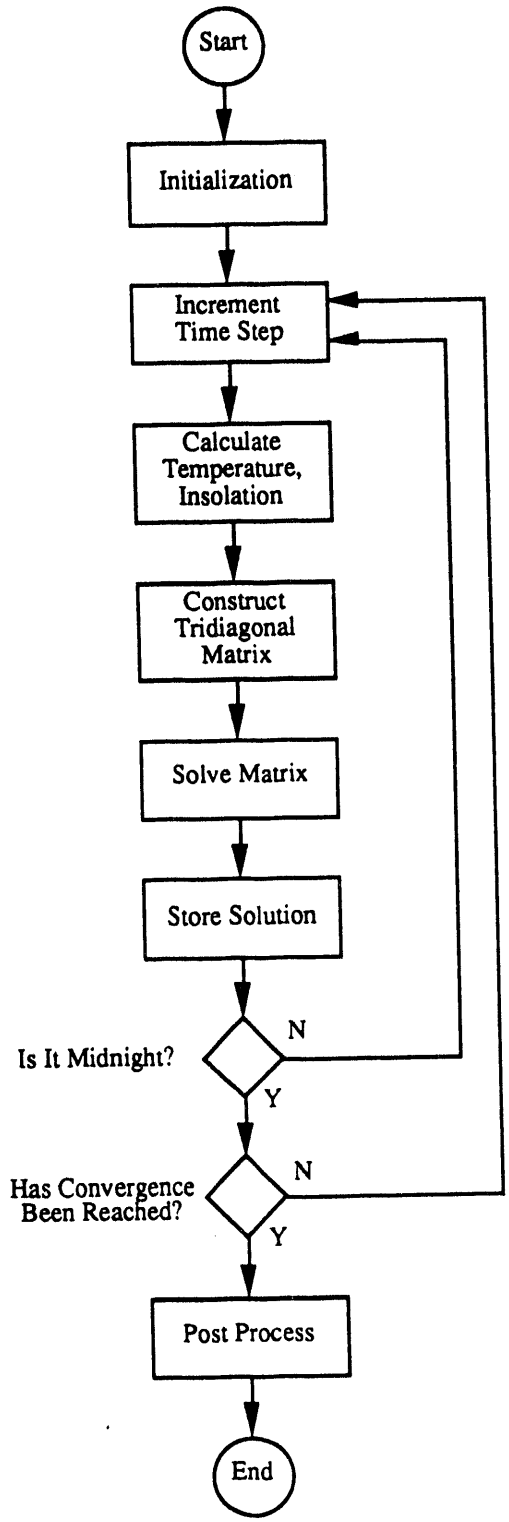

Figure 8. Flow Chart of Solution Procedure

4.0 VALIDATION AND BENCHMARKING

The computational procedure just described must be verified to ensure the correctness of its derivation as well as its implementation. Two benchmark problems having analytical solutions have been examined. The first benchmark problem addressed is a simple semi-infinite slab, initially at a uniform temperature t_0, that is exposed to a convective heat transfer process on its exposed surface. Given the ambient temperature, t_∞, and the convection coefficient, h, as well as the material properties of the slab, k and α, the temperature response in the slab after some finite time, $\Delta\tau$, may be calculated from an analytically derived formula.

The second benchmark problem concerns the same semi-infinite slab, again exposed to convection heat transfer, but in this case the ambient temperature, t_∞, varies sinusoidally with a given period, ω. An analytical expression for the temperature variation within the slab exists as a function of time and distance into the slab. Each of the two benchmark problems will be discussed at length, and a comparison of the numerical and analytical solutions will follow in the subsequent sections. Figure 9 depicts the general arrangement of both benchmark problems.

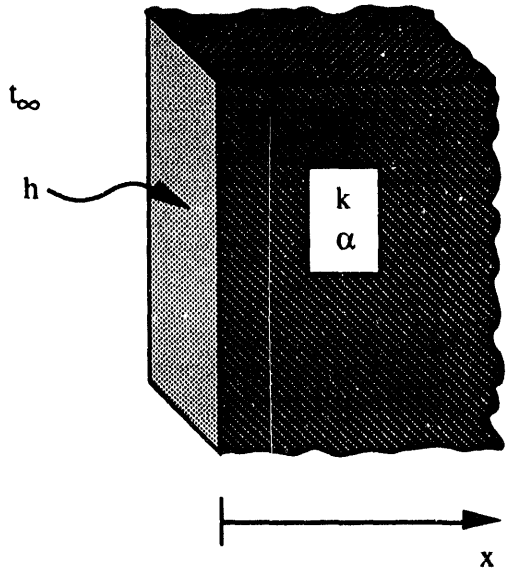

Figure 9. A Semi-Infinite Slab Exposed to Convection

4.1 Semi-Infinite Constant-Temperature Convection Transient

The semi-infinite slab of Figure 9 is initially at temperature t_0. At time $\tau = 0$, the slab is exposed to a convective heat flux at the surface $x = 0$. This heat flux is proportional to the difference between the surface temperature $t(0,\tau)$ and the constant ambient temperature, t_∞. To establish a convention for the direction of the heat flux, it will be assumed that $t_\infty > t_0$, such that heat flows into the slab. The slab material has a constant thermal conductivity, k, and a constant thermal diffusivity, α. Furthermore, the convection coefficient, h, is given and is constant. The expected solution will be an asymptotic approach to the ambient temperature for any point within the slab. It is anticipated that the time constant for the approach to the ambient temperature will be a function of the distance into the slab: the closer to the surface a point is, the faster its temperature will increase.

The expected form of the solution is confirmed by the analytical solution. The analytical solution to this problem is presented in Gebhart (Gebhart, 1993). The temperature solution as a function of time, τ, and position, x, is given as:

$$\frac{t(x,\tau) - t_0}{t_\infty - t_0} = \text{erfc}\left(\frac{x}{2\sqrt{\alpha\tau}}\right) - \exp\left(\frac{hx}{k} + \frac{h^2}{k^2}\alpha\tau\right)\text{erfc}\left(\frac{x}{2\sqrt{\alpha\tau}} + \frac{h}{k}\sqrt{\alpha\tau}\right) \tag{33}$$

Figure 10 presents a plot of the behavior of the analytical solution at several different values of time, τ, along with the numerical solutions at the corresponding times, calculated for a discretization with $\Delta x = 0.05$ m, and $\Delta\tau = 100$ s. These calculations were performed for a semi-infinite slab of steel: $k = 60.5$ W/m/K, $\alpha = 1.77\times10^{-5}$, $h = 10.0$ W/m^2/K. To simplify interpretation of the temperature $t(x,\tau)$, the value of $t_0 = 0.0$, and $t_\infty = 1.0$ so the nondimensional temperature is equivalent to the calculated $t(x,\tau)$. Figure 10 shows excellent agreement of the analytical and numerical solutions.

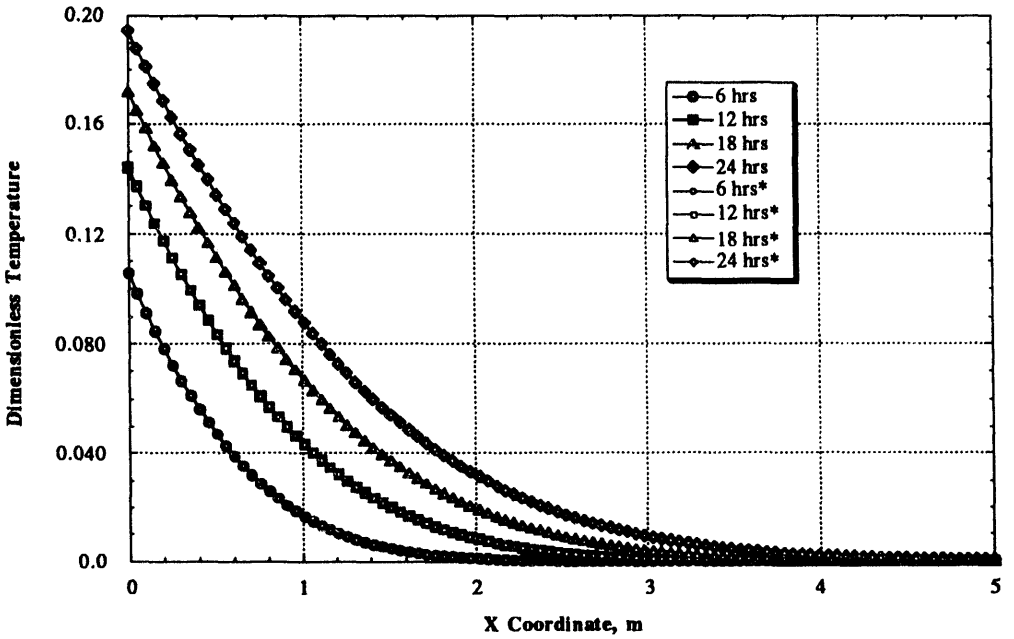

Figure 10. Plot of Numerical and Analytical (*) Solutions of the First Benchmark Problem

Figure 11 displays a plot of the L2 error norms of the entire numerical solution over the full domain of space and time (5 m in the x-direction, 24 hr in time, τ). The error is calculated as a function of spatial discretization, for several values of time step, by the following equation:

$$\| t_a - t_n \|_2 = \frac{\Delta\tau\ \Delta x}{X\ T}\sqrt{\sum_{j=1}^{M}\sum_{i=1}^{N}\left[t_a(x_i,\tau_j) - t_n(x_i,\tau_j)\right]^2} \tag{34}$$

The values X and T represent the spatial and temporal domain of the computation, the subscripts a and n denote the analytical and numerical solutions, respectively, and the subscripts i and j represent the ith node and the jth time step. Figure 11 demonstrates the convergence of the algorithm for a sufficiently small time step, and it is evident that the scheme will continue to approach the analytical solution as the number of nodes is increased and the time step is decreased. One notable feature of Figure 11 is the increase in the L2 error norm when the spatial discretization is more refined than the temporal discretization. This increase in error is due to the propagation of temporal error into the spatial solution. For simulations performed with large time steps, the calculated solution is only an approximation of the analytical solution. As the spatial discretization is continually refined, the algorithm calculates a more and more exact spatial representation of an *incorrect* solution and hence ,the error increases beyond a certain point. This effect can be combated, however, by ensuring that a sufficiently small time step is used for whatever spatial discretization is implemented.

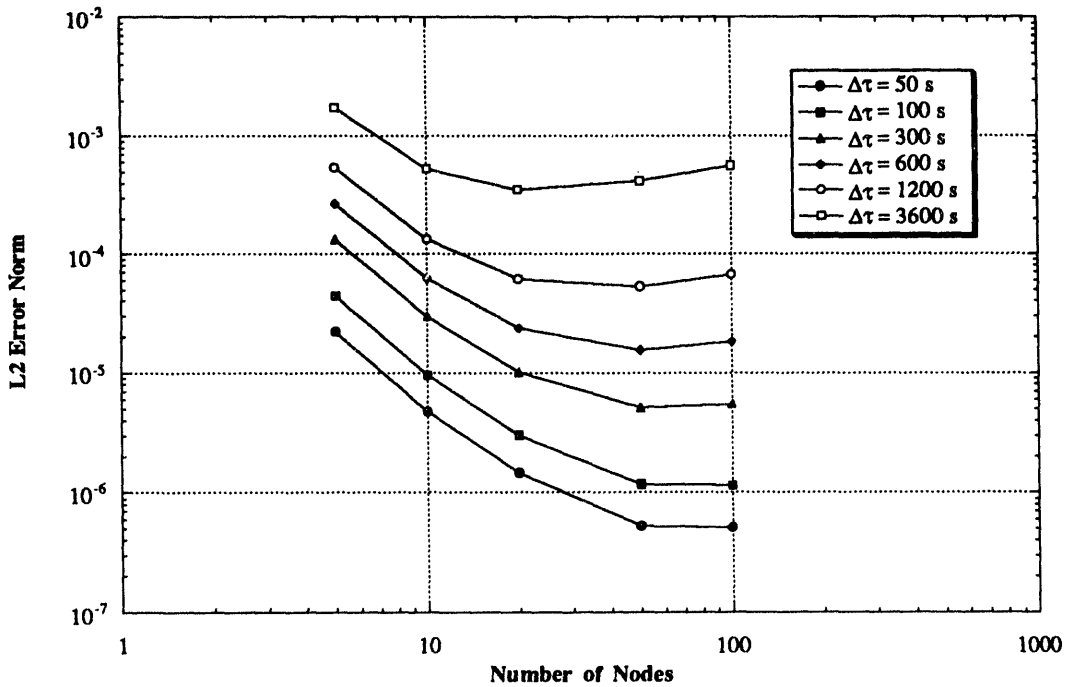

Figure 11. Plot of the L2 Error Norm for the First Benchmark Problem as a Function of Spatial Discretization for Various Time Steps

For each of the above solutions, the semi-infinite slab is approximated by a slab 5 m in width, but the simulations are not carried out past the time that temperature variations propagate beyond this distance. It is evident that this does not occur until well past the 24-hr solution shown in Figure 10.

4.2 Semi-Infinite Sinusoidal Convection Transient

In this simulation, the semi-infinite slab of Figure 9 is exposed for a long period of time to a fluid whose temperature, t_∞, is sinusoidally varying with time. The equation representing this temperature oscillation is defined as:

$$t_\infty(\tau) = \bar{t} + t_a \cos(\omega\tau) \tag{35}$$

The amplitude of the variation is given as t_a, and its frequency is ω. The slab is initially at the mean temperature of the fluid, $\bar{t}$ throughout, so that the transient temperature approaches a constant value of $\bar{t}$ as x approaches infinity, irrespective of time. Material properties in this problem are the same as those defined for the previous benchmark problem. The slab material has a constant thermal conductivity, k, thermal diffusivity, α, and a convection coefficient, h. The expected solution is a sinusoidally varying temperature whose amplitude decays with position in the slab. Furthermore, the sinusoidal behavior within the slab should exhibit a phase lag behind the ambient temperature.

The analytical solution confirms the expected form of the solution. Gebhart again presents the analytical solution to the problem (Gebhart, 1993). The temperature solution as a function of time, τ, x position, and the frequency of the oscillation, ω, is given as:

$$t(x,\tau) = \bar{t} + a\, t_a \exp\left(-x\sqrt{\frac{\omega}{2\alpha}}\right)\cos\left(\omega\tau - x\sqrt{\frac{\omega}{2\alpha}} - b\right) \tag{36}$$

where

$$a = \sqrt{\frac{1}{2c^2 + 2c + 1}}$$

$$b = \arctan\left(\frac{c}{c+1}\right) \qquad (37)$$

$$c = \sqrt{\frac{k\omega\rho c_p}{2h^2}}$$

The behavior of the analytical and corresponding numerical solutions are shown in Figure 12 for several different values of time, τ, calculated for a discretization with $\Delta x = 0.0025$ m and $\Delta\tau = 100$ s. These calculations were performed for a semi-infinite slab of steel, $k = 60.5$ W/m/K, $\alpha = 1.77 \times 10^{-5}$, $h = 10.0$ W/m^2/K. The values needed to specify the ambient temperature, t_∞, are $\bar{t} = 300.0$ K, $t_a = 10.0$ K, and $\omega = 2\pi$ x 24 hr. The phase of the ambient temperature is specified such that the peak ambient temperature occurs at noon.

The plot in Figure 12 exhibits several features of note. It can be observed that, of the four times shown, high levels of heat flux into and out of the surface ($x = 0$) occur at noon and midnight, respectively. This is evident because high heat flux into the slab will result in a large negative gradient in temperature near the surface of the slab. Furthermore, when the ambient temperature has returned to 300 K at both 6 A.M. and 6 P.M., the surface flux is near zero (the slope of the temperature at the surface is approximately zero), due to the small temperature difference between the ambient fluid and the steel slab. Figure 12 also demonstrates the level of accuracy of the computational algorithm, as at most points the numerical simulation cannot be distinguished from the analytical solution. For this benchmark case, the semi-infinite slab is approximated by a slab 5 m in width; the data presented in Figure 12 demonstrates graphically that significant temperature variations do not propagate beyond this distance.

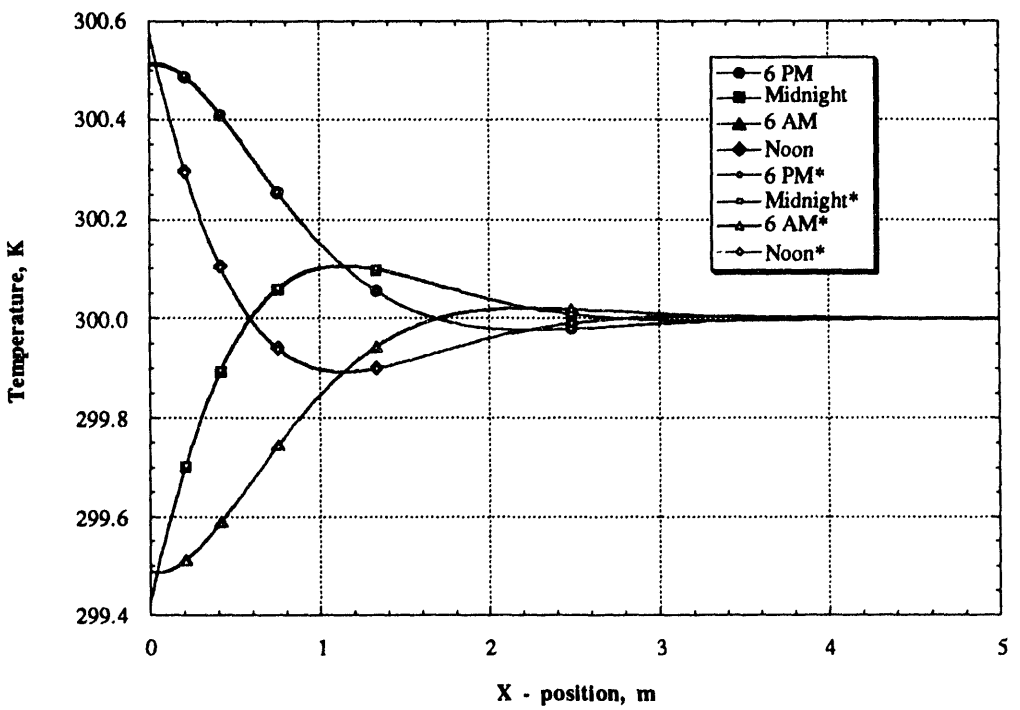

Figure 12. Plot of Numerical and Analytical (*) Solutions of the Second Benchmark Problem

Figure 13 shows the L2 error norm of the entire numerical solution in space and time (over an entire 24-hr cycle, and for the entire slab). The L2 norm of the error is again defined as:

$$\| t_a - t_n \|_2 = \frac{\Delta\tau \, \Delta x}{X T} \sqrt{\sum_{j=1}^{M} \sum_{i=1}^{N} [t_a(x_i,\tau_j) - t_n(x_i,\tau_j)]^2} \qquad (38)$$

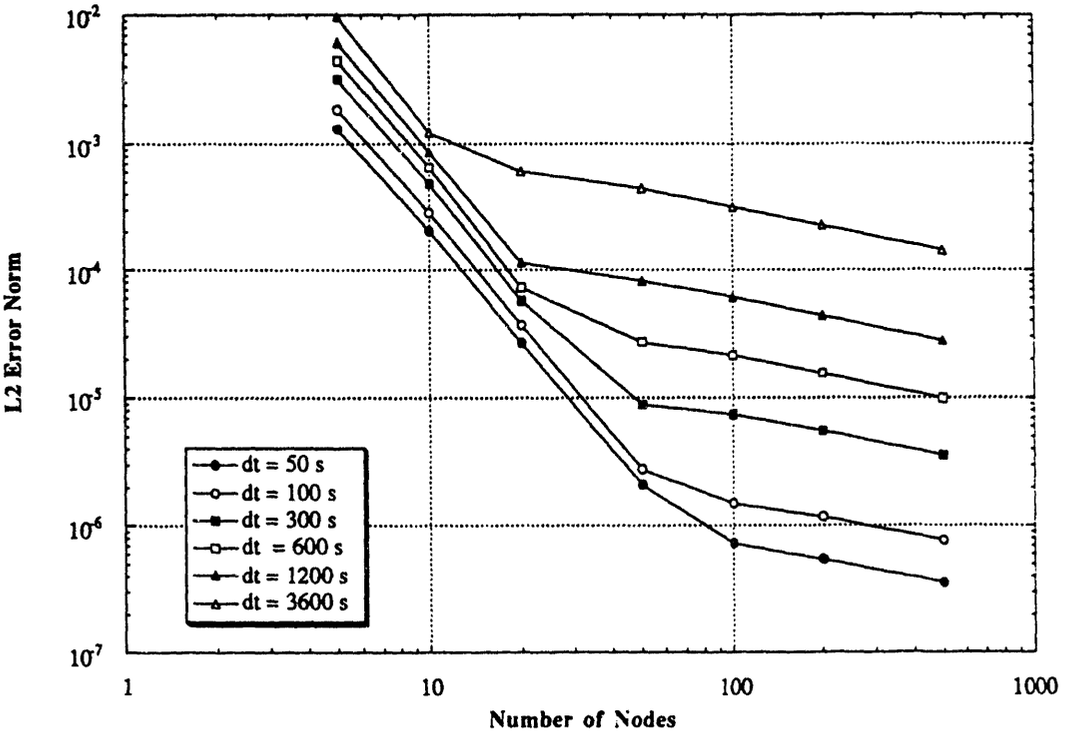

Figure 13. Plot of the L2 Error Norm for the Second Benchmark Problem as a Function of Spatial Discretization for Various Time Steps

The values X and T again represent the total length and time of the computation, respectively (5 m and 24 hr), and the subscripts a and n denote the analytical and numerical solutions, respectively. The L2 norm error is calculated as a function of spatial discretization for several time steps. Figure 13 demonstrates the convergence of the algorithm, and suggests that the scheme will approach a single solution (equal to the analytical one) through subsequent refinement of spatial and temporal discretization. The problem of unmatched spatial and temporal discretizations, which was evidenced in Figure 11 for the first benchmark, does not arise here because of the periodicity of the solution. The second benchmark problem is not susceptible to temporal error propagation because the continual repetition of the boundary conditions allows this type of error to die away with time. The temporal error effectively becomes part of the residual, which is forced to a small value by the convergence criterion. The temporal error is seen to propagate into the spatial solution; however, this effect is manifested in the form of a decrease in the magnitude of the slope of the error curve in Figure 13 when the spatial discretization is more refined than the temporal discretization. It is reassuring to note that the error increase of Figure 11 will not arise in the solutions of the normal day problems that are presented in the subsequent section, due again to the periodic nature of these problems, and the opportunity for error diminution that is afforded by the residual minimization and convergence scheme.

5.0 RESULTS

The computational method developed in the foregoing portions of this report was used to compare the thermal effects that the realistic diurnal ambient temperature and insolation cycle caused, to the thermal condition resulting from the application of the regulatory ambient condition of 10 CFR 71 for *two* typical cask configurations. These cask configurations were examined to determine the values of emissivity of the shield and cask surface that resulted in the most compromising temperature profile comparison. These tests were then used to establish a base case analysis to which all subsequent runs are compared. Series of calculations were then made to determine the effect of planar geometry, neutron shield material, neutron shield thickness, and convection coefficient on the solutions for the two general configurations. These calculations are detailed in ensuing discussions in this report. A description of the general cask geometries follows.

Since current spent fuel shipping cask designs are of two general types and sizes as dictated by the two major methods of transportation, road and rail, it was determined that examination of a generic truck cask (TC) as well as a generic rail cask (RC) was in order. The generic truck cask is based on the General Atomics GA-4 design (GA Report #910353/0), and a schematic diagram of the wall design appears in Figure 14. The cask wall of this design consists of five laminations, three of stainless steel (SS1), and one each of depleted uranium (DU) and polypropylene (POLY). The stainless steel serves primarily as structural support, while the polypropylene is a neutron shield, and the depleted uranium acts as a gamma barrier. Figure 14, while not to scale, shows the dimensions of the cask wall as implemented in the subsequent analyses.

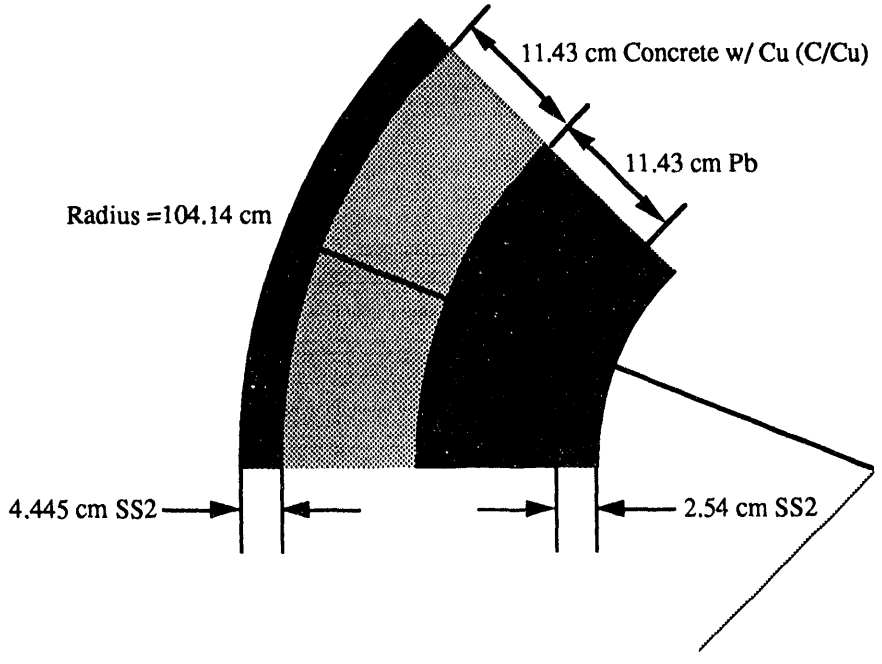

Drawing not to Scale

Figure 14. Schematic Drawing of Generic Truck Cask Wall

The rail cask configuration is shown in Figure 15, and is based on the Babcock & Wilcox BR-100 design (B&W Report #51-1203400-01). The RC wall consists of four laminations, two of which are a slightly different alloy of stainless steel from that used in the TC, hereafter referred to as SS2. The neutron shield of the RC is composed of concrete containing copper fins (denoted subsequently as C/Cu) to aide the transfer of heat away from the spent fuel. The gamma shield is lead (Pb). The dimensions of the various laminations as well as the cask radius, appear in Figure 15.

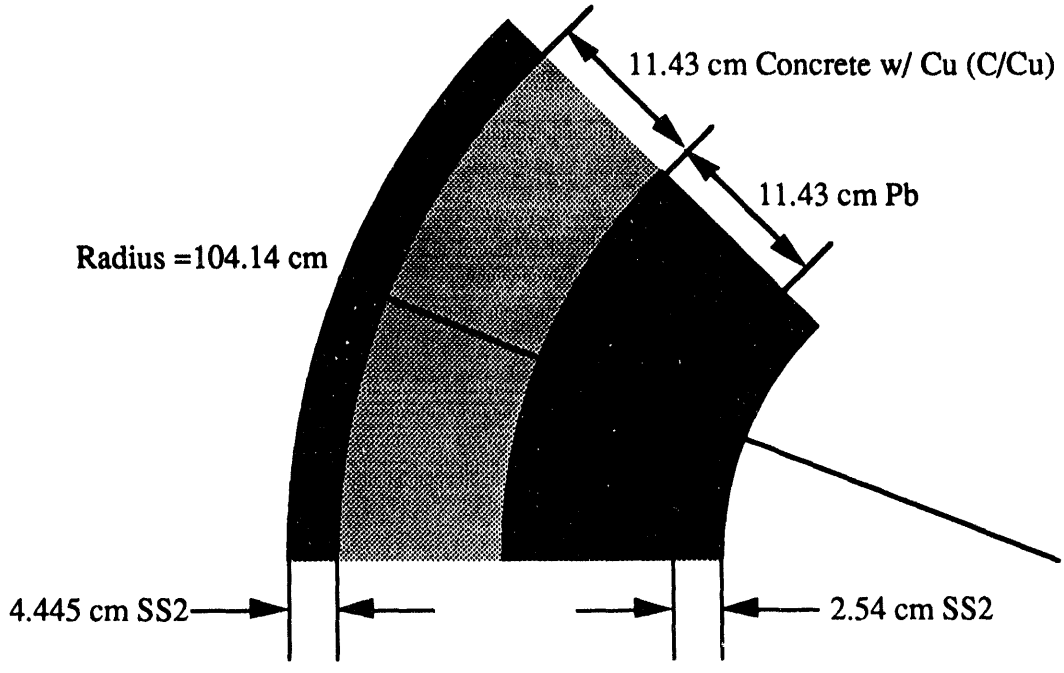

Drawing not to Scale

Figure 15. Schematic Drawing of Generic Rail Cask Wall

The thermal properties of the various materials are central to the analysis which follows, so they are given explicitly in Table 3. Table 3 also includes thermal properties for two neutron shield materials that will be used in a later portion of this report, those of liquid water (H_2O), nominally at 300 K, and plain concrete, without copper fins (CNF). A variety of other data are necessary in order to run the computer code as described. These quantities and their assumed values are identified in Table 4. Justification of each of the assumed values is discussed below.

Table 3. Thermal Properties of Materials

	Thermal Conductivity (W/m/K)	Density (kg/m^3)	Heat Capacity (J/kg/K)	Thermal Diffusivity (m^2/s)
SS1	13.85	7888.7	460.44	3.813×10^{-6}
SS2	15.95	8027.0	502.3	3.956×10^{-6}
DU	25.54	19293	131.85	1.004×10^{-5}
Pb	35.13	11340	125.57	2.467×10^{-5}
POLY	0.1454	941.11	1925.5	8.024×10^{-8}
C/Cu	16.45	1849.0	2164.0	4.111×10^{-6}
H2O	0.613	997.01	4179.0	1.471×10^{-7}
CNF	1.40	2300.0	880.0	6.917×10^{-7}

Table 4. Additional Parameters

Parameter	Value
Initial Temperature Profile	350 K
Convection Coefficient	10 $W/m^2/K$
Interior Flux	100 W/m^2
Convergence Criterion	0.01 K/Day
Time Step	10 s

The initial temperature profile, as stated previously, is arbitrary because the code is run until the convergence criterion is met, at which time all residual effects resulting from the choice of initial condition will have died away. The value of 350 K was chosen in order to minimize the computational time needed to reach the converged state.

The convection coefficient, h = 10 $W/m^2/K$, is a frequently cited value for natural convection from horizontal plates (Brown et al., 1992) (Incropera and DeWitt, 1981). However, since the convection coefficient governs the ease that heat leaves the solar shield, it is expected that large variations in h may have significant effects on the behavior of the cask surface when comparing the regulatory and realistic solutions. A brief study will be undertaken subsequently to determine the extent of this effect.

The interior heat flux arises due to the decay heat of the spent fuel inside the container. While the RC is expected to have much more spent fuel, and hence much greater decay heat production than the TC, 100 W/m^2 is applied uniformly to the regulatory and realistic simulations. Because of the uniform and constant nature of this parameter, it is expected that while a variation in decay heat load will change both the realistic and regulatory solutions, it will change them proportionately so that the comparison of the two sets of ambient conditions will not be changed when the decay heat varies.

The convergence criterion and time step are purely computational parameters that also apply uniformly to the regulatory and realistic simulations; however, since they directly affect the accuracy of the simulations, it is important that they are well specified. The convergence criterion is chosen to be 0.01 K in variation when the result at midnight is compared to the result exactly 24 hr earlier. This value is

sufficiently small to ensure that large-scale transients have diminished and the solution has reached a steady diurnal variation.

The time step is 10 s, a value shown to be sufficiently small for the spatial discretization (approximately 300 nodes) in the foregoing benchmarking section. The radiation linearization is also most accurate for small time steps; a time step of 10 s fixes the maximum temperature variation at less than 0.1 K per step, which in turn results in errors of less than 0.05% for the linearization. Finally, it is noted that using a 10 s time step, in combination with a convergence criterion of 0.01 K per day results in a step-to-step convergence level of less than 2.0×10^{-6}, a very restrictive condition, which in some cases took the algorithm more than 30 simulation days to reach.

5.1 Shield Results

The emissivities of the cask surface and the solar shield are not well known quantities, as emissivity may vary considerably with material type and surface characteristics. It is expected that, in general, emissivities of the cask surface and shield will exist in the range 0.3 to 1.0. Furthermore, because the emissivity is intimately coupled to the heat transfer between the cask surface, the solar shield, and the environment, it is expected that varying the emissivities will have a similar effect to varying the convection coefficient. Differences in the emissivities will cause a variation in the importance of the transient behavior to the overall maximum temperature profile, which may change the behavior of the realistic solution significantly when compared to the regulatory solution. This is demonstrated below.

Figure 16 shows the bounding temperature profiles of the realistic simulation throughout the wall of the TC, and the profile that results from application of the regulatory condition of 10 CFR 71, for the simulation involving cask and shield emissivities equal to 1.0. Similar plots are shown in Figure 17 for grey surfaces with emissivities both equal to 0.3. The *realistic* profiles are calculated by monitoring the temperatures throughout the problem domain on the final, converged day of the simulation, and without regard to time of day, recording the minimum and maximum temperatures for each node in the solution. The regulatory condition is truly steady-state, so no such bounding solutions are necessary. The maximum, minimum, and regulatory values of the ambient temperature and shield temperature are also displayed in the plot; however, little attention should be paid to the x-coordinates of these data points, as their spatial positions are not strictly specified. The relative positions of these points are correctly represented, as the $x = 0.0$ position corresponds to the cask surface so the shield is at a position less than zero, and the ambient condition is even further to the left. These data points are included in all subsequent plots, where applicable, but will no longer be explicitly labeled.

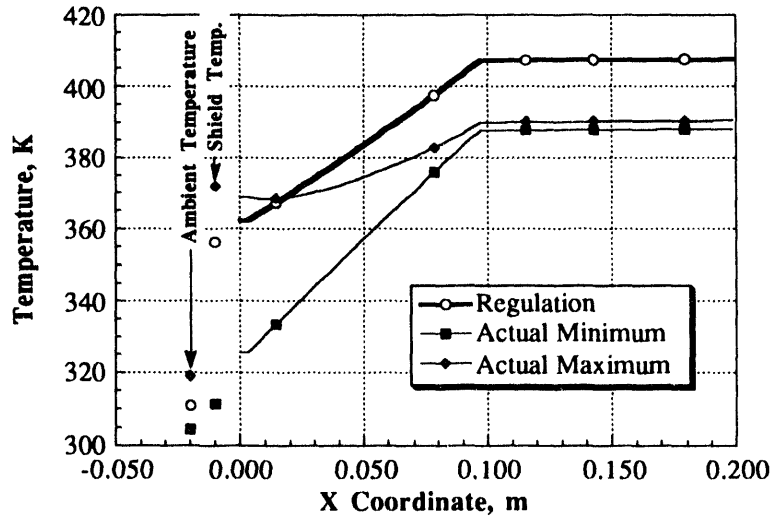

Figure 16. Truck Cask, Black Shield, Black Surface

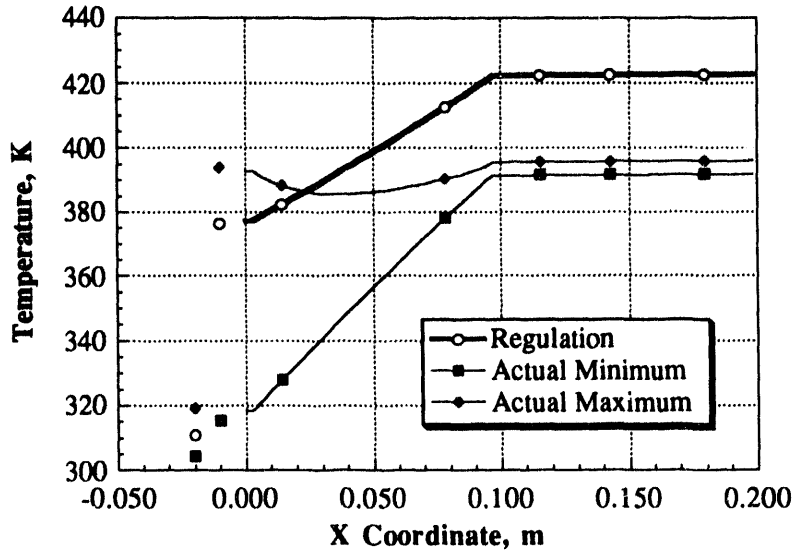

Figure 17. Truck Cask, Grey Shield, Grey Surface

It is crucial to point out that although these calculations have been carried out with very realistic ambient conditions and cask designs, one critical component of these calculations is considered arbitrary with regard to the intended focus of this analysis. As described earlier, the application of the heat load emanating from the spent fuel will not change the relative profiles of the realistic and regulatory cases even if the heat load is varied drastically. However, variation of the heat source will change the magnitudes of the temperatures within the cask walls quite significantly. Thus it must be noted that the temperature profiles calculated for discussion is this section are to be viewed only with regard to comparisons of the relative effects of the realistic and regulatory conditions, and should not in any way be construed as predictions of actual *temperatures* in transport situations. Therefore, if any specific temperature within any cask wall is shown as exceeding the specific regulatory guidelines for the temperatures of corresponding cask components, this must not be taken as a weakness of the cask design, the computational algorithm, or of this analysis. The calculations that demonstrate compliance with specific temperature regulations are the domain of cask manufacturers and are wholly outside the scope of this report.

The general behavior demonstrated in Figure 16 is typical of most solutions for the TC. The amplitude of the diurnal thermal wave is illustrated by the bounding minimum and maximum curves. It can be seen that the amplitude of the thermal wave decreases sharply in the region corresponding to the POLY neutron shield. This is due to the wave-attenuating effect of materials with small thermal conductivities. Similarly, the slope of the curve increases dramatically through this same region, also due to the low conductivity of the POLY. The immediately obvious information demonstrated by Figure 16 is that, for at least part of the day, the temperature in the outer regions of the cask wall exceeds the temperature that is predicted when the regulatory condition is applied. However, in the regions inside the neutron shield, and for most of the neutron shield itself, the maximum temperature is bounded by the regulatory condition. This behavior is reiterated in Figure 17; however, a noteworthy feature of Figure 17 is that the region where the maximum temperature exceeds the regulatory one is slightly larger than for the black case of Figure 16.

Figures 18 and 19 are also calculations using the TC configuration, but for cases of a grey shield and black surface, and black shield and grey surface, respectively. The goal of performing analyses on all these permutations of shield and surface emissivities is to find the case in which the maximum portion of the cask wall is exposed to temperatures exceeding the regulatory calculation. It is evident from comparing Figures 16 through 19 that while all four cases exhibit similar characteristics, the worst case

is that illustrated in Figure 19, a TC with a black shield and a grey surface. This case seems not only to involve the largest portion of cask above the regulatory temperature, but also to involve the smallest margin of compliance in the interior region of the cask, where the maximum temperature is somewhat less than 20 K below the regulatory condition, in comparison to 20 to 30 K for the other cases. The term "margin of compliance" refers to the temperature difference that the regulatory solution exceeds the realistic solution at the interior boundary of the cask wall. Thus Figure 19 is identified as the base case for the remainder of the TC analysis, since it represents something of a worst-case scenario for the emissivity conditions. The temporal variation of this base case will be examined subsequently.

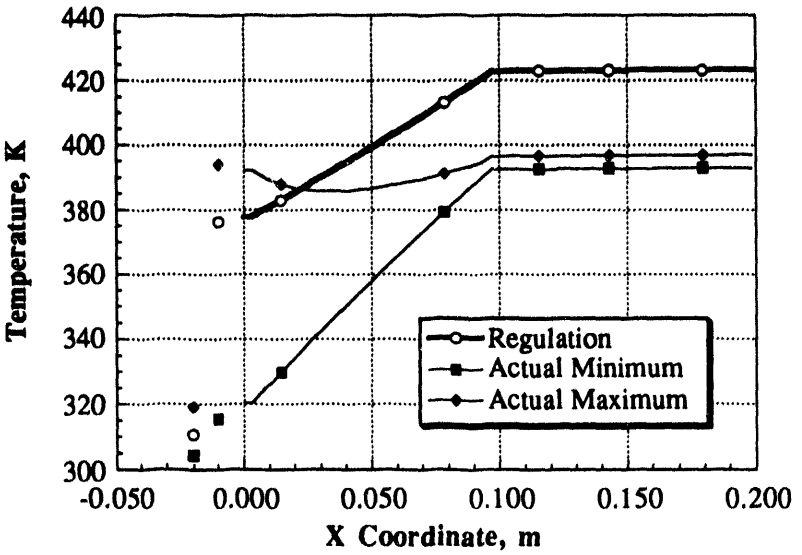

Figure 18. Truck Cask, Grey Shield, Black Surface

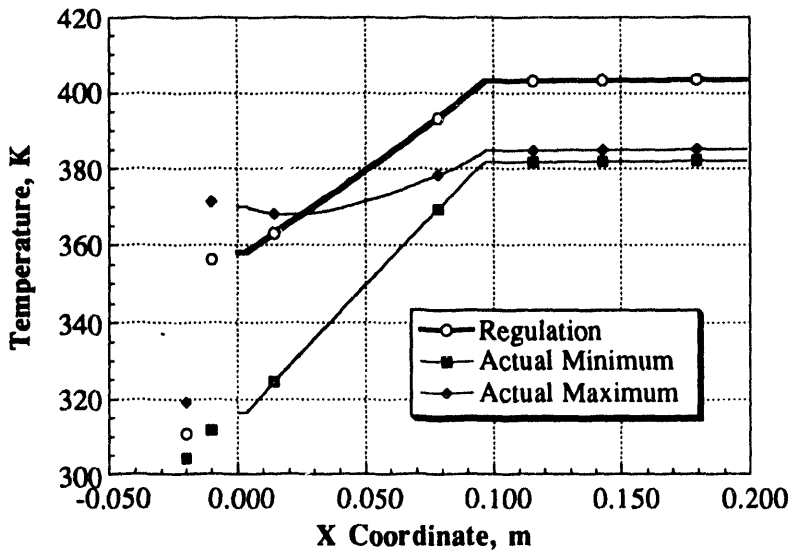

Figure 19. Truck Cask, Black Shield, Grey Surface

Figures 20 through 23 were derived by performance of the identical set of permutative analyses for the RC of Figure 15. This set of figures exhibits remarkably different characteristic temperature profiles as compared to those of the TC discussed previously. The rather high thermal conductivity of the C/Cu neutron shield leads not only to a decrease in the thermal wave attenuation of the wall, but it also allows the entire mass of the cask wall to absorb the energy associated with the thermal waves. The end result of these phenomena is that the entire cask wall lies below the calculated regulatory profile. The only place that the realistic maximum exceeds the regulatory profile is at the solar shield itself, and only for the black case (Figure 20). Also of note is the very small slope of the temperature profiles in each of the figures; this a direct result of the high thermal conductivity across the entire wall. Comparing the compliance margins of the various cases again reveals that the black shield, grey surface case of Figure 23 has the smallest margin, about 12 K compared to 14 to 20 K for the other cases. The black shield, grey surface case is therefore identified as the base case for subsequent RC analysis.

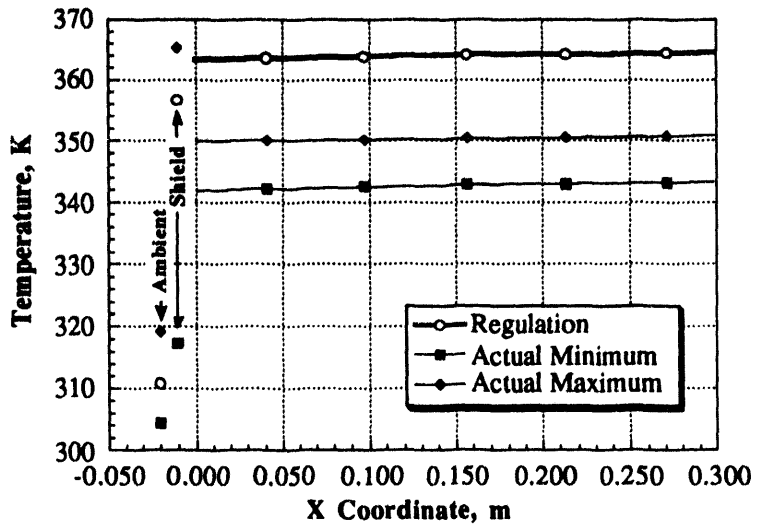

Figure 20. Rail Cask, Black Shield, Black Surface

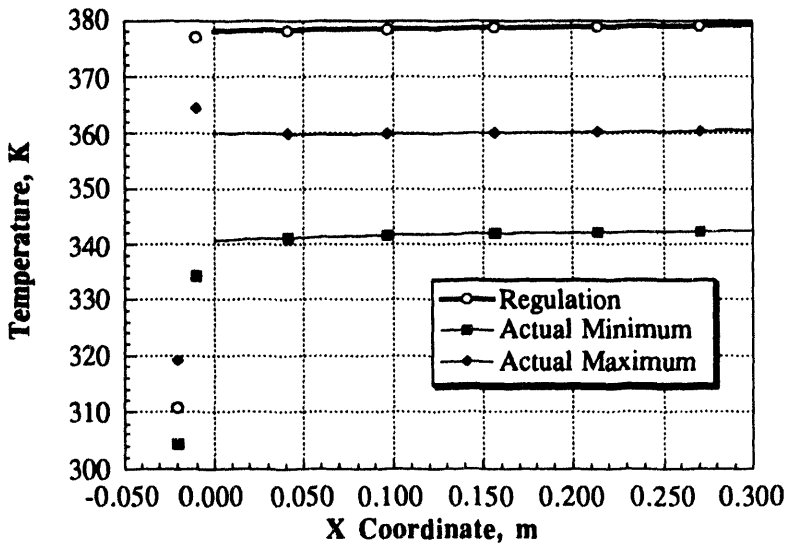

Figure 21. Rail Cask, Grey Shield, Grey Surface

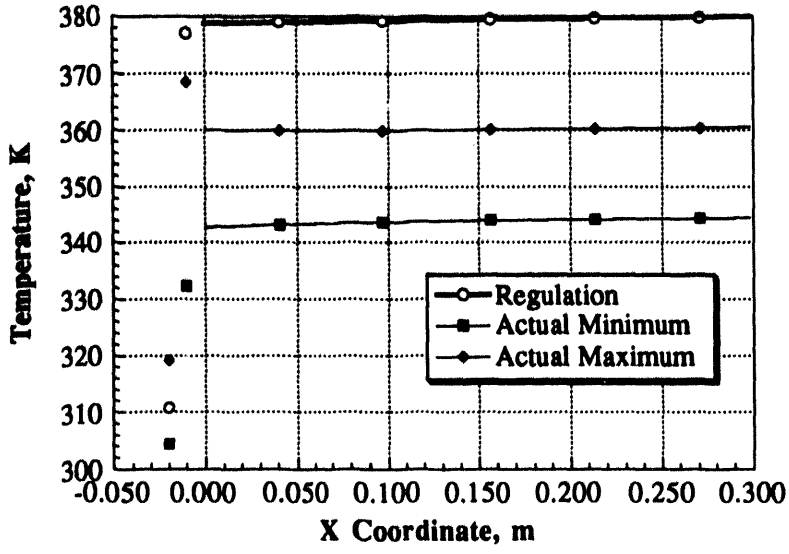

Figure 22. Rail Cask, Grey Shield, Black Surface

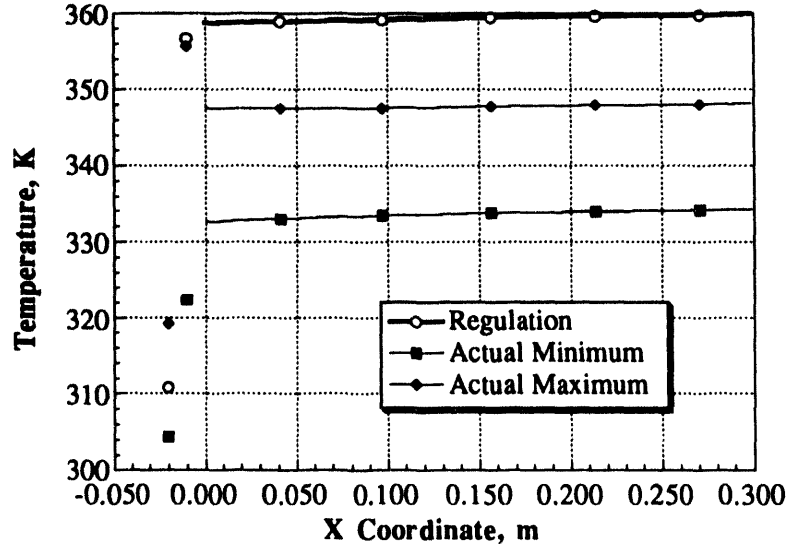

Figure 23. Rail Cask, Black Shield, Grey Surface

Figures 24 and 25 show the results of similar calculations performed for the TC and RC, respectively, this time without any solar shield. These computations were performed in order to demonstrate the limiting nature of the base case scenarios. It is observed in Figure 24 that the temperature profile across the wall is similar to those previously calculated, and that the maximum does not exceed the regulation in as much of the neutron shield as the base case; furthermore, the margin of compliance on the interior is well over 25 K. Figure 25 is much like the previous RC figures, and it is observed that the margin is approximately 17 K, so the shielded case is far more severe.

Having confirmed the two base cases (one each for the TC and RC), these cases will be examined temporally in order to more explicitly demonstrate the meaning of the spatial plots.

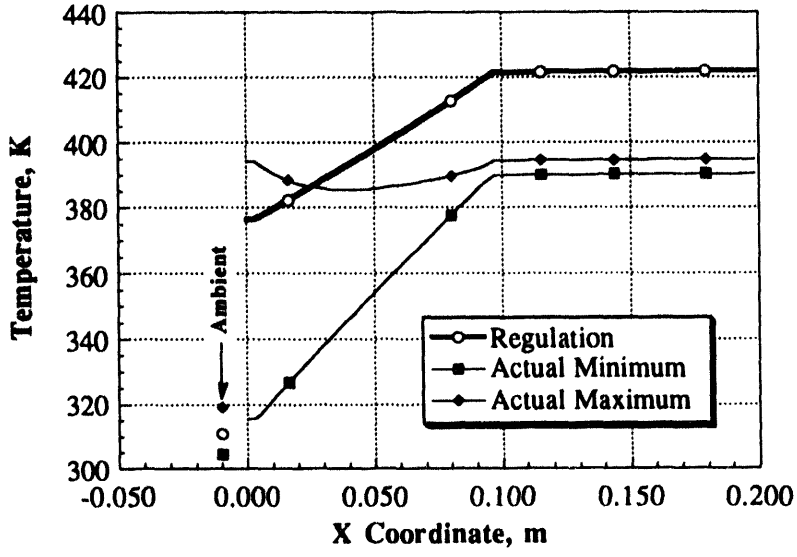

Figure 24. Truck Cask, No Shield, Grey Surface

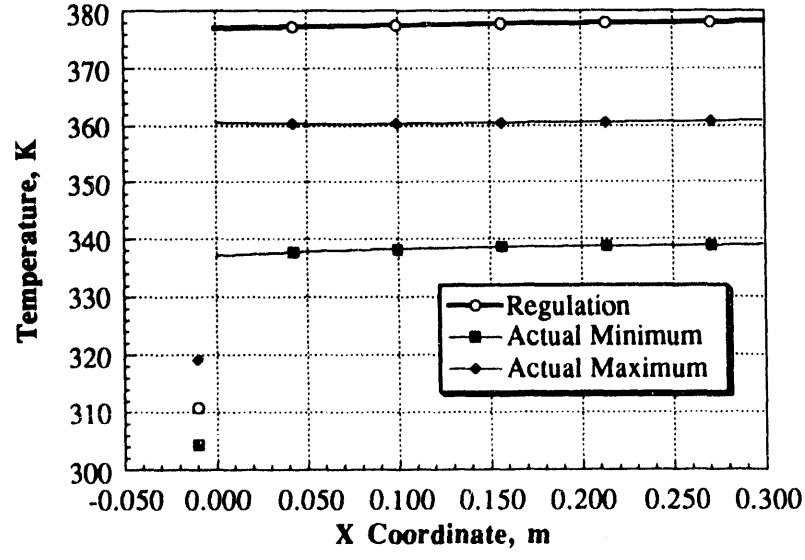

Figure 25. Rail Cask, No Shield, Grey Surface

5.2 Base Results

To illustrate how the temperature profiles of the previous section were generated, and to further demonstrate the base-case analyses, Figures 26 and 27 have been produced. Each of these figures shows the variation of temperature over a full 24 hr for the ambient condition, solar shield, cask surface and cask back face for the regulatory and realistic conditions. Figure 26 presents this data for the generic truck cask, Figure 27 the rail cask.

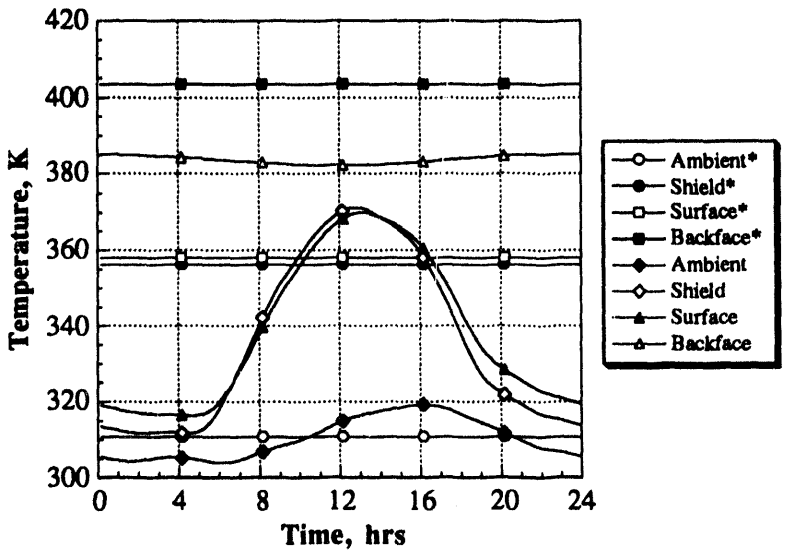

Figure 26. Truck Cask, Base Case, Diurnal Variation for Realistic Simulation and Regulatory Conditions (*)

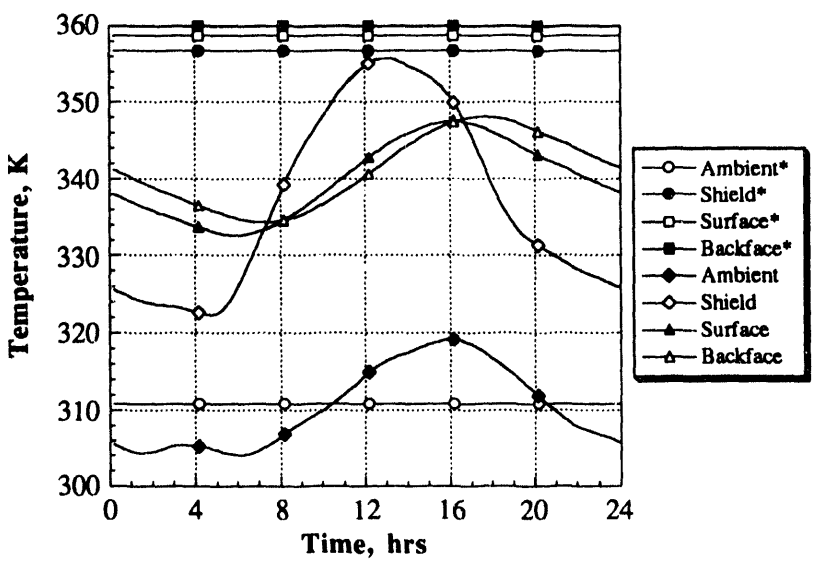

Figure 27. Rail Cask, Base Case, Diurnal Variation for Realistic Simulation and Regulatory Conditions (*)

It is interesting to note in Figure 26 that the peak shield temperature occurs just after noon, solar time, while the ambient temperature peak is at 4 P.M. This indicates that insolation dominates the environmental heat transfer effects, and that the high solar flux is strictly responsible for the brief period the shield and cask surface exceed the regulatory solution. The cask surface is seen to vary essentially in phase with the solar shield temperature. This is due to the inability of the surface to permeate thermal energy freely to the greatest portion of the thermal mass of the cask, due to the insulating neutron shield. The plot in Figure 26 also demonstrates that the back face never exceeds the regulatory solution in the base case. Furthermore, the peak back face temperature occurs at approximately midnight, which implies that the thermal waves require a full 12 hr to propagate through the TC wall.

Figure 27 demonstrates explicitly some of the key features of the RC wall design. The main feature of the RC, its higher thermal conductivity neutron shield, causes two major changes in the phase shift of the propagating thermal waves. First, the ability of the cask surface to communicate with the entire cask wall thermal mass allows the peak temperature of the surface to occur about 3 hr after the peak solar shield temperature.

Additionally, the back face temperature is now more closely in phase with the surface temperature, with a phase lag of about 2 hr, because of the small time constant of the composite wall. The importance of these effects is that the entire cask wall absorbs and diminishes the effect of the diurnal transient, so that the surface temperature is now much lower than the regulatory temperature, at all times.

5.3 Geometry Results

As the computational algorithm has been written in a form that allows calculations to be performed in either Cartesian or radial coordinates, a calculation of each base case has been performed in order to judge the relative importance of the geometrical scheme to the solution. Figures 28 and 29 display the planar geometry solutions for the base cases of the TC and RC, respectively. The differences between these figures and the radial base cases (Figures 19 and 23) are rather slight. The major difference is that in both plots the temperatures across the entire profile are lower in the radial case. This effect is explained by the fact that in the radial case the heat transfer area increases as one proceeds outward from the internal boundary where the flux condition is enforced. The increase in area forces a decreased gradient for the same heat rate; therefore, temperatures in the interior are lower in radial geometry than in planar geometry, where the heat transfer area is constant throughout the wall.

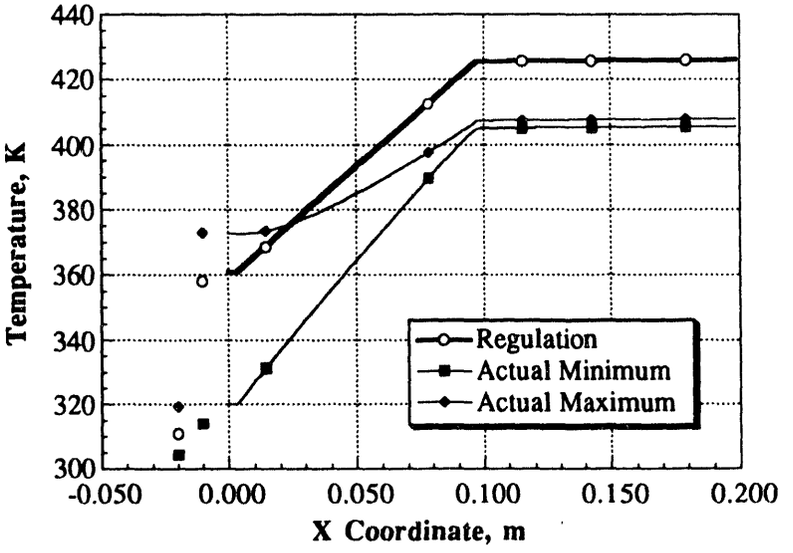

Figure 28. Truck Cask, Base Case, Planar Geometry

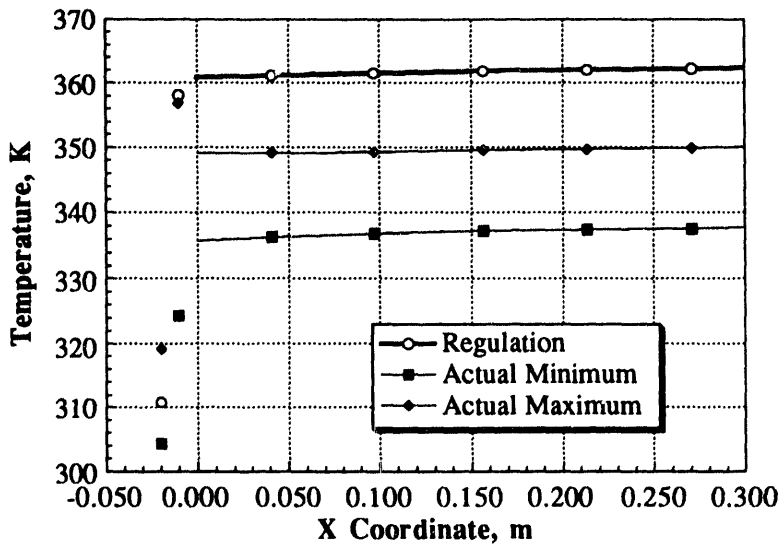

Figure 29. Rail Cask, Base Case, Planar Geometry

While the specific temperature values and gradients are seen to increase, the feature of interest, namely the relative behavior of the maximum and regulatory temperatures, goes largely unchanged in the planar geometry results. In Figure 28, the TC plot, the maximum and regulatory temperature profiles cross in nearly the same location as in Figure 19, and at the interior the temperature difference is essentially the same, slightly less than 20 K. Similar observations can be made in comparing Figures 29 and 23. The temperature differences are practically identical throughout the cask, although there is some small difference in the thermal gradients due to the change in geometry, which accounts for the rather insignificant differences in the compliance margin.

5.4 Materials Results

Transportation of commercial spent nuclear fuel has not yet begun in earnest. While several cask designs have been finalized, others may yet be contemplated. To prepare for the possibility of cask designs that do not resemble the generic TC or RC designs already presented, this section and the subsequent one will investigate the use of alternative cask wall configurations. Since the neutron shield has been identified as the key component dictating the thermal response of the cask to ambient conditions, this section will concentrate on the use of different types of neutron shield and evaluate their impact on the comparison between realistic and regulatory ambient conditions. These evaluations are oversimplified by their failure to take into account the neutron attenuation factor of each material. In fact, it is assumed for the purpose of these calculations that the thickness of each material is the same, thus maintaining the original geometry, and only varying material properties. The impact of variations in the thickness of the neutron shield will be discussed in a subsequent section.

Beginning with the TC model described previously, analyses were made replacing the POLY neutron shield with C/Cu, H_2O, and CNF in turn. The temperature profiles resulting from these calculations are found in Figures 30, 31, and 32, respectively.

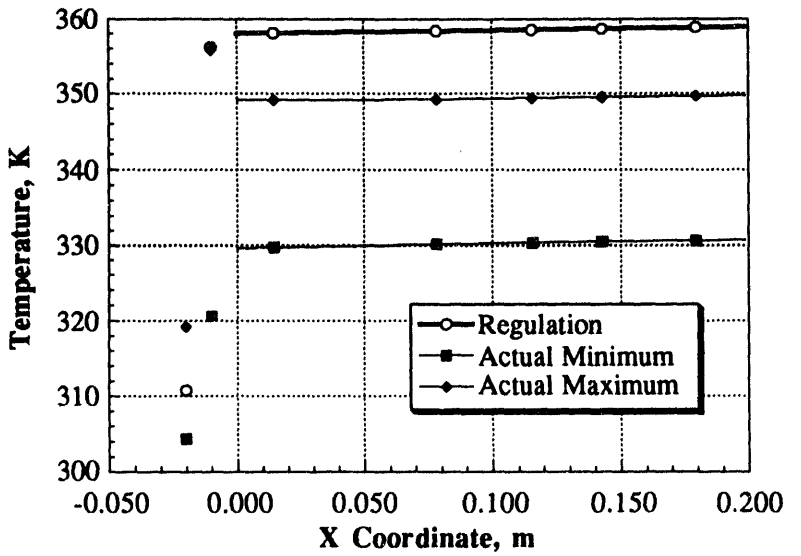

Figure 30. Truck Cask, C/Cu Neutron Shield

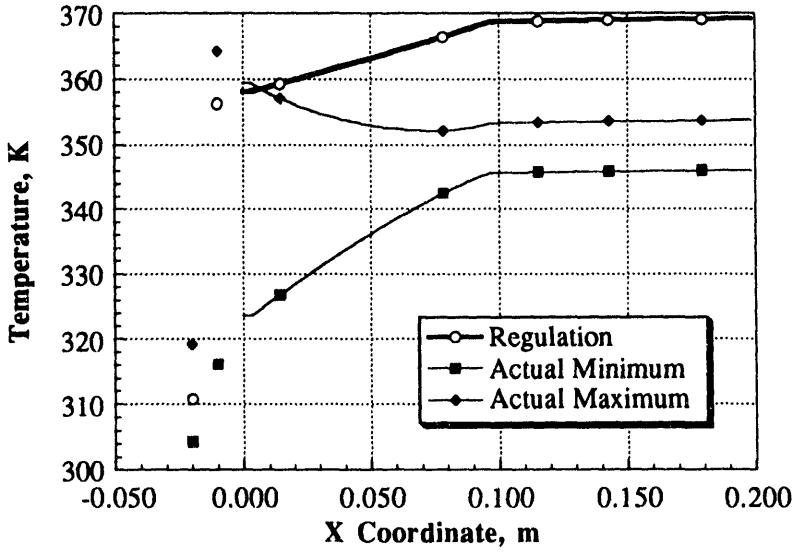

Figure 31. Truck Cask, H_2O Neutron Shield

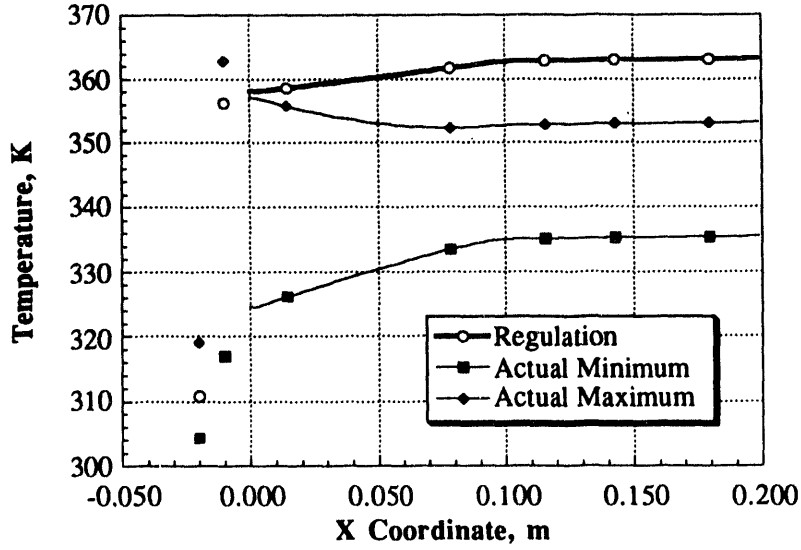

Figure 32. Truck Cask, CNF Neutron Shield

Figure 30, the TC with a C/Cu shield, has a profile very similar to the base case for the RC. This is strictly due to the use of the same neutron shield. It is obvious from this example that the use of C/Cu will ensure that temperatures in a realistic simulation for a TC will not exceed those calculated under the steady-state regulatory condition. The use of water, depicted in Figure 31, shows that while shield and surface temperatures for the TC may lie above the regulatory condition, in general the response is more favorable than that calculated when using the nominal POLY neutron shield. Figure 32 demonstrates that the use of plain concrete as the neutron shield in the TC also results in maximum temperatures lower than the regulation, except for at the solar shield, where the peak temperature exceeds the regulation, presumably during the early afternoon. Because all of the alternative neutron shields compare favorably to the base case, when shield thicknesses are varied subsequently, the original POLY shield will be examined.

The RC geometry was also revisited, this time with POLY, H_2O and CNF neutron shields, in Figures 33, 34 and 35. Figure 33 depicts the solution for the generic RC design with an equal thickness of POLY neutron shield substituted for the original C/Cu one. It is evident that the regulatory condition and realistic conditions produce nearly identical maximum temperatures through the steel shell at the surface, and that interior realistic temperatures are less than the regulation throughout. The main difference between this thermal profile and that of the TC base case is that the 4-cm steel shell at the surface is capable of storing much more heat than the 0.5-cm shell of the TC. The storage capacity allows depression of the peak temperature to levels much closer to the regulatory value. This effect was observed by Brown in the study of steel plates of varying thickness (Brown et al., 1992). When H_2O and CNF are substituted for the C/Cu neutron shield, the results are quite similar. In these cases, depicted in Figures 34 and 35, the maximum solar shield temperatures do exceed the regulation solution; however, throughout the entire wall the maximum temperatures are well below the regulatory solutions. In the interest of performing an increased level of analysis on one of the other possible shield materials in the RC configuration, the CNF shield will be examined in the subsequent section in order to determine the effect of varying the shield thickness on the cask response. The concrete shield was chosen because the POLY shield will be studied in the TC configuration, and liquid water is not as likely a candidate for actual use in RC designs. Furthermore, it seems well established that the C/Cu shield has no difficulties in complying with the corresponding regulatory solution. This leaves the CNF shield as the best choice for further work.

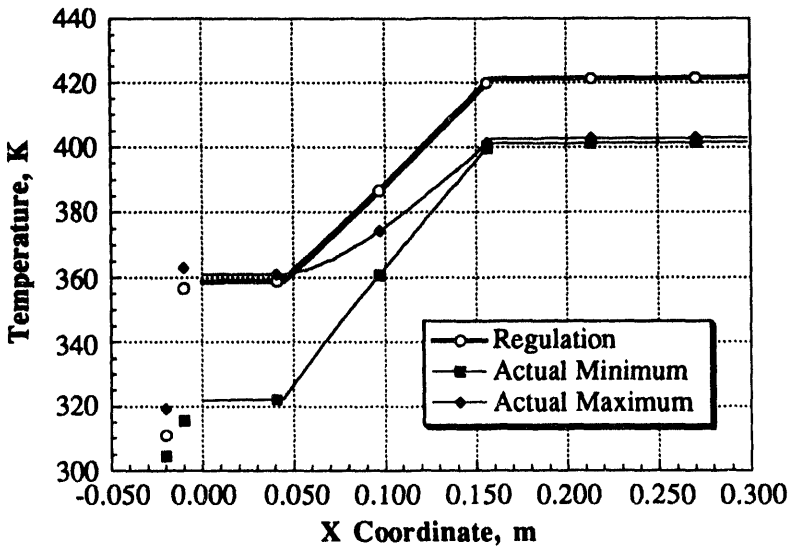

Figure 33. Rail Cask, POLY Neutron Shield

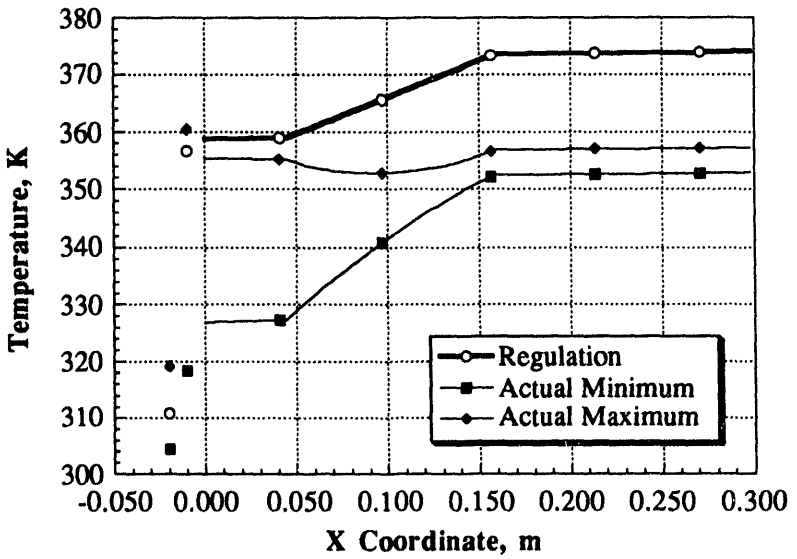

Figure 34. Rail Cask, H_2O Neutron Shield

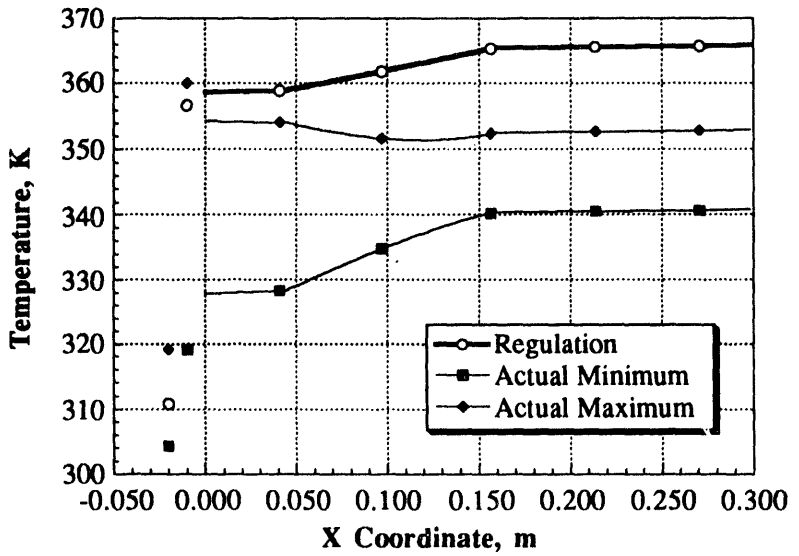

Figure 35. Rail Cask, CNF Neutron Shield

5.5 Neutron Shield Thickness Results

This section shows the result of varying the neutron shield thickness. It has been demonstrated that the neutron shield is the most fundamental component in the determination of the overall cask thermal response to diurnal ambient conditions. It has also been shown that the neutron shield material has a great impact on the cask response. Having selected two materials for examination in the two cask configurations, it remains to demonstrate the dependence of the cask response upon neutron shield thickness. The analyses have been performed by varying the neutron shield thickness while maintaining the cask wall thickness as a whole. The outer layer of steel is kept at its *original* dimension, so that when the neutron shield thickness is increased, the interior laminations (steel and gamma shield) get smaller, but stay in proportion to one another. Nine cases were performed for each cask configuration, and the results of these cases are plotted in Figures 36 through 40.

Since it has already been demonstrated that the areas of interest for these cask designs are the solar shield and cask surface, as the interior temperatures invariably meet the regulatory condition, the temperature differences at these locations are plotted as a function of neutron shield thickness. Figure 36 displays the difference between the maximum shield temperature as calculated in the realistic simulation and under the regulatory condition. The cask is of the TC design, with a POLY neutron shield whose thickness is varied between 2.0 cm and 17.0 cm. The temperature difference is at a maximum between 6.0 and 7.0 cm; however, the most notable fact is that the temperature difference does not vary much over the specified range of thicknesses. This suggests the conclusion that regardless of its thickness, once POLY shielding has been chosen for use in the given TC configuration, a maximum temperature disparity of around 15 K will exist at the solar shield. The plot in Figure 37 shows the temperature disparity at the cask surface, and it shows the same behavior as Figure 36, but with a typical temperature difference of 12 K. Because the regulatory and maximum temperature profiles are seen to cross in the outer layers of the neutron shield, a plot of the distance into the shield at which the crossing takes place versus shield thickness was thought to be of value. Figure 38 identifies the thickness of neutron shield material in which the maximum temperature exceeds the regulatory solution. This value is seen to peak at 2.2 cm for a 9-cm POLY shield and dwindle slowly for shields of larger thicknesses.

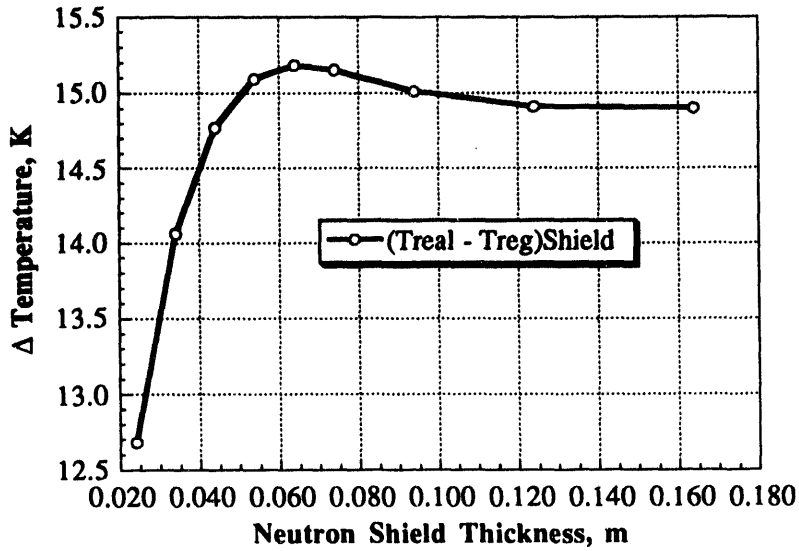

Figure 36. Truck Cask, Variation of POLY Thickness, Temperature Difference at Solar Shield

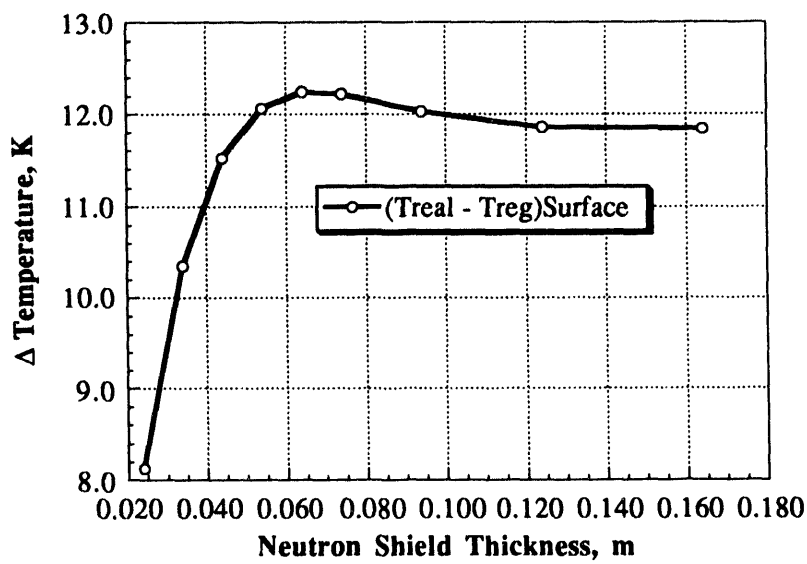

Figure 37. Truck Cask, Variation of POLY Thickness, Temperature Difference at Cask Surface

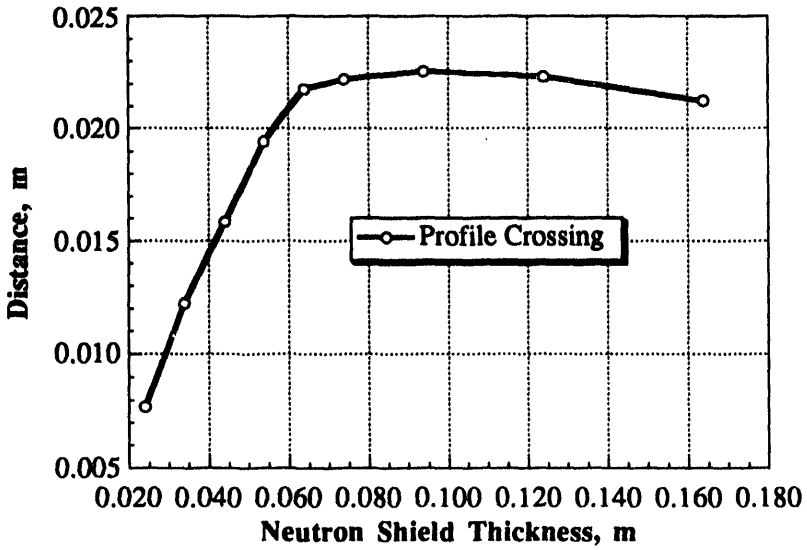

Figure 38. Truck Cask, Variation of POLY Thickness, Thickness of POLY Breached by Maximum Profile

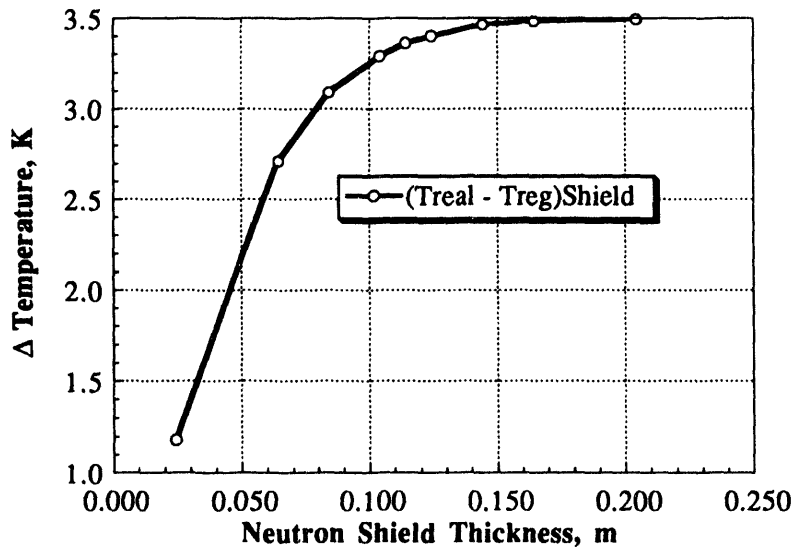

Figure 39. Rail Cask, Variation of CNF Thickness, Temperature Difference at Solar Shield

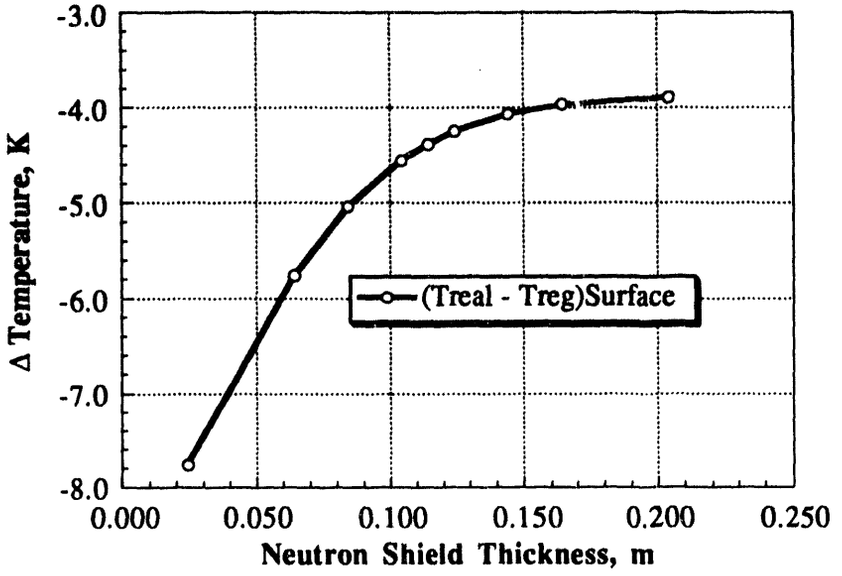

Figure 40. Rail Cask, Variation of CNF Thickness, Temperature Difference at Cask Surface

Figure 39 shows the variation of solar shield temperature difference for the RC configuration with a neutron shield of CNF. The peak temperature difference of 3.5 K in the plot occurs at 20 cm of shield material and continues to increase slowly from there. The feature of note is how little the temperature difference actually varies (1.0 - 3.5 K) with large changes in the shield thickness (2 - 25 cm). In Figure 40 the temperature difference at the cask surface is plotted. In this plot, the values of temperature difference are negative because the maximum surface temperature is lower than the regulatory solution. Because the surface temperature is in compliance, the temperature profiles do not cross, hence no analog of Figure 38 can be plotted for the RC.

5.6 Convection Results

In order to demonstrate the variation of the difference in temperature profile of the maximum and regulatory solutions with respect to convection coefficient, h, Figures 41 and 42 have been created. These figures plot the difference between the maximum and regulatory solutions ($t_{max\ real} - t_{reg}$) at the solar shield, cask surface, and the back face of the cask wall. The simulations were performed for the TC and RC base configurations, for h = 1, 10, and 100. Figure 41 shows that the TC surface and shield will not exceed the regulatory calculation by more than 15 K and that the back face will never be in violation over this large range of convection coefficients. It is observed that the temperature differences of Figure 42 are fairly linear when plotted against the logarithm of the convection coefficient. Extrapolation of the curves allows the prediction that the cask wall maximum temperature will exceed the regulatory profile for values of h just greater than 100 W/m^2/K. This is appropriate, because large values of h mean that the oscillating ambient temperature waves are permeated with great ease into the wall interior. The case of a high h value, however, is not conservative from the perspective of heat dissipation; therefore, in actual cask design analyses, it is expected that small values of h will be used, and so these analyses will not be susceptible to inadequate regulatory conditions.

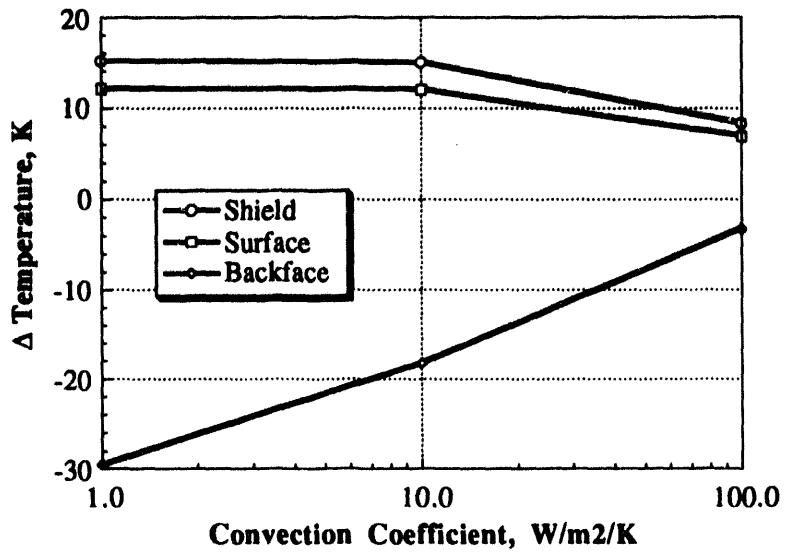

Figure 41. Truck Cask, Variation of Temperature Difference Versus Convection Coefficient

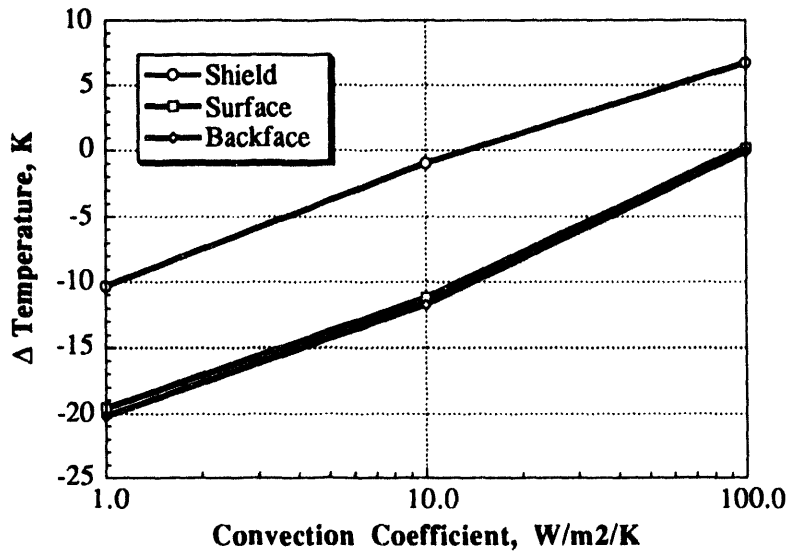

Figure 42. Rail Cask, Variation of Temperature Difference Versus Convection Coefficient

6.0 CONCLUSIONS

The previous sections of this report describe the development of a computational method for use in the transient thermal analysis of spent fuel shipping container walls. This method was developed in order to compare the effects of the 10 CFR 71 specified normal day conditions with those effects caused when a container is subjected to realistic thermal conditions that might be present on a hot day in the contiguous United States. The body of the report develops in detail the specification of these realistic hot day conditions, the way that they were applied to the numerical model, and the benchmarking of that model. Finally, the report presents and interprets the results of many numerical analyses that were performed in order to compare the effects of the 10 CFR 71 normal conditions with those instigated by the realistic hot day conditions. In this section, these results will be summarized, conclusions will be drawn, and recommendations will be made as to the course of future study and to the suggested use of the data presented here.

6.1 Results Summary

Simulations were performed in order to gauge the effect of variations in the cask and shield emissivity, the removal of the solar shield, the use of planar geometry, the use of different neutron shield materials, the variation in width of the neutron shield, and the variation of the convection coefficient. All these simulations were performed on two different generic cask designs: the TC of Figure 14 and the RC of Figure 15.

A base case for the TC was selected by determining the worst combination of solar shield and surface emissivities; therefore, all subsequent evaluations were performed with a black solar shield and a grey cask surface. In general, the TC was found to respond to the realistic conditions in such a way that the solar shield and the layer of stainless steel on the surface of the cask exceeded the temperatures predicted by the regulatory condition for a period of about 4 hr during the afternoon. At some point within the POLY neutron shield, however, the regulatory and maximum realistic temperature profiles were seen to cross and the remainder of the interior of the wall was well below the temperature predicted when the regulatory condition was applied, regardless of the time of day. This general statement of the result applies to *every* case involving the TC (whether varying the convection coefficient, changing to Cartesian geometry, or the thickness of the POLY shield), except when the neutron shield material was changed. When the neutron shield material was varied, it was found that the poly shield was the worst scenario, as in this case the greatest amount of wall thickness was at a higher temperature than the regulatory calculation.

The RC design was also found to have a single, generally applicable result. Because of the superior thermal conductivity of the RC's C/Cu neutron shield, the heat conduction pathway was found to be nearly isothermal with respect to the spatial coordinate. Furthermore, the *entire* cask wall was found to vary in temperature in a range well below the regulatory solution. The single exception to this generalization was at the solar shield itself where, for a few cases, the temperature during a short period in the afternoon was found to exceed the regulatory calculation. When the neutron shield material was varied the same result was found except when the shield was changed to POLY, where results resembling the TC were encountered. Finally, it was found that for convection coefficients larger than 100 $W/m^2/K$ the entire RC cask wall may exceed the regulatory solution for some portion of the day.

6.2 Conclusions

The simulations performed in the course of this analysis have consistently and uniformly shown that the *interior* maximum wall temperatures of both the TC and RC fall well below those predicted when the regulatory normal conditions of 10 CFR 71 are used. It has been shown that maximum temperatures near the surface of some cask designs and at the solar shield occasionally lie slightly above the regulatory prediction. These temperature differences are small enough that it is expected that normal conservative allowances will correct for any potential violations. Furthermore, it is pointed out that the "realistic" conditions used in this study contain some degree of embedded conservatism as the temperature condition and the insolation condition are taken from two different locations, each the worst case out of all the

available data. This means that while either condition may be encountered in principle, both conditions have never been observed to occur simultaneously. This conservativity enforces the calculated solutions as worst case limitations.

The analyses have made it clear that diurnal temperature variations that penetrate the cask wall all have maxima substantially less than the corresponding regulatory solutions. Therefore it is certain that vital cask structural components located interior to the neutron shielding and the spent fuel itself will not exceed the temperatures calculated by use of the conditions of 10 CFR 71. However, this is not necessarily the case with regard to the outer regions of the cask wall. Therefore, some caution must be used in the evaluation of cask designs where external temperatures predicted using the 10 CFR 71 conditions are close to regulatory limits. Particularly of interest is the temperature restriction involving the accessible surface of the cask. Care must be taken to ensure that proper levels of conservatism are used in such calculations, or it is conceivable that actual casks that meet the accessible surface limitation under the regulatory normal day conditions may fail to meet the same condition under circumstances involving real days with extreme temperatures and high insolation levels.

Finally, the key factor in determining the cask response to ambient conditions is the material composition of the neutron shield. Unlike typical structural materials (metals), and gamma shields (heavy metals), neutron shields can be made of a large variety of materials, having a wide range of thermal properties. Investigations using four potential shield choices, POLY, C/Cu, H_2O and CNF, revealed a large variation in cask response between the materials. Furthermore, it was found that POLY is the most limiting case as it may cause external transient temperatures to exceed those calculated using the regulatory normal condition by the largest margin observed, although *internal* temperatures remain below those predicted for the regulatory condition.

6.3 Recommendations

Since this study was concerned primarily with evaluation of the generic TC and RC designs and the variations in these designs that were derived by replacing the neutron shield materials, it is conceivable that a radical departure from the considered designs or neutron shield materials may make the conclusions of this work tenuous. However, if the cask material thermal properties are no poorer than those of POLY, and the cask consists of concentric cylindrical or planar laminations, it is quite likely that the phenomena observed in this study are directly applicable to the situation of interest. In the absence of such design departures, it is recommended that additional realistic analyses not be performed. Such calculations are burdensome, and as this evaluation has shown, unnecessary, because the differences between the maximum realistic temperature and the regulatory profile are much smaller than typical conservative assumptions. Hence, it is recommended that the results of this study be considered valid until cask designs using inapplicable geometries or materials are proposed. At such time, the computational algorithm used here may be easily adapted to undertaking additional studies.

7.0 REFERENCES

B&W Report #51-1203400-01, "100 Ton Rail/Barge Spent Fuel Shipping Cask," Babcock and Wilcox, November, 1991.

Brown, N. N., S. E. Gianoulakis, and W. H. Lake, "Comparison of 10 CFR 71 Normal Day Conditions With Bounding U. S. Hot Day Extremes," (SAND91-2255C) Sandia National Laboratories, Albuquerque, NM, 1992.

GA Report #910353/0, "Legal Weight Truck From Reactor Spent Fuel Shipping Cask, Final Design Report," General Atomics, November 1991.

Gebhart, B., Heat Conduction and Mass Diffusion, McGraw-Hill Inc., 1993.

Gringorten, I. I., A. J. Kantor, Y. Izumi, and P. I. Tattelman, Section 15.1: *Handbook of Geophysics and the Space Environment*, 1985.

IMSL MATH Library, Version 1.0, April 1987.

Incropera, F. P. and D. P. DeWitt, Fundamentals of Heat and Mass Transfer, Second Edition, John Wiley & Sons, 1981.

Lake, W. H., "Modeling the Normal Thermal Environment," Proceedings of the 6th International Symposium on Packaging and Transportation of Radioactive Materials, pp. 1090-1097, West Berlin, November 10-14, 1980.

Press, W. H., B. P. Flannery, S. A. Teukolsky, and W. T. Vetterling, Numerical Recipes, FORTRAN Version, Cambridge University Press, 1989.

Typical Meteorological Year User's Manual, TD-9734, National Climatic Data Center, Asheville, NC, 1981.

APPENDIX A: SOURCE CODE LISTING

```
      program insolation
c
c     Solves a one dimensional transient conduction problem
c     with radiation/convection boundary condition.  Utilizes
c     Semi-implicit linearization of Stefan-Boltzmann equation.
c     Simulates a container with multiple layers of materials.
c     Radiation and Temperature Data culled from the Typical
c     Meteorological Year compiled by the National Climatic Data
c     Center.  Radiation for the maximum global insolation to a
c     tilted surface.  Temperature Data From TMY for Yuma, Arizona,
c     7/10
c
c
c     Steven J Manson
c
c     July, 1993
c
c*********************************************************************
c
      implicit double precision (a-h,o-z)
c
c     Parameters Defined:
c
c     il = Number of Layers of Different Materials
c     im = Maximum Number of Nodes in any Layer
c
      parameter (il = 5, im = 500, two = 2.0d0,one = 1.0d0,
     +           zip = 0.0d0)
c
c     Array Definitions:
c
c     x(i,j) = the spatial coordinate of the jth node in the ith layer
c     t(i,j) = the temperature of the jth node in the ith layer, K
c     t24(i,j) = the temperature of the ith,jth node at midnight, K
c     tmin(i,j) = the minimum t of the ith,jth node during current day
c     tmax(i,j) = the maximum t of the ith,jth node during current day
c     n(i) = the number of nodes in the ith layer
c     con(i) = the thermal conductivity of the ith layer, W/m/K
c     alf(i) = the thermal diffusivity of the ith layer, m2/s
c     wid(i) = the width of the ith layer, m
c     dx(i) = the node spacing in the ith layer
c     r1(i,j) = the inverse of the radial position of the i,j node, m
c     sr(k) = the kth fourier cosine coef of the radiation heat flux
c     st(k) = the kth fourier cosine coef of the external temperature
c     a,b,c,f,z = matrices necessary for solution of the implicit
c                 heat conduction equation
c
      dimension x(il,im),t(il,im),con(il),alf(il),wid(il),n(il),
     +  dx(il),a(il*im),b(il*im),c(il*im),f(il*im),z(il*im),
     +  t24(il,im),tmin(il,im),tmax(il,im),sr(48),st(48), r1(il,im)
      logical shield
c
c     Initiate Preprocessor
c
```

```
      write(*,*)' preprocessing'
      call prep(il,im,x,t,n,con,alf,wid,a,b,c,f,z,dx,nn,
     +          conv,maxday,dt,ill,h,flux,sr,st,r1,shield,tsh,ec,es)
c
c     Solve Conduction until Steady Variation Achieved
c
      write(*,*)' processing'
      call proc(il,im,x,t,n,con,alf,wid,a,b,c,f,z,dx,nn,
     +          conv,maxday,dt,ill,h,flux,t24,tmin,tmax,
     +          sr,st,r1,shield,tsh,ec,es,tshmin,tshmax)
c
c     Postprocess Results
c
      write(*,*)' postprocessing'
      call post(il,im,x,t,n,tmin,tmax,ill,tshmin,tshmax)
c
c
      stop
      end
c
c
c*********************************************************************
c
      subroutine prep(il,im,x,t,n,con,alf,wid,a,b,c,f,z,dx,nn,
     +        conv,maxday,dt,ill,h,flux,sr,st,r1,shield,tsh,ec,es)
c
c*********************************************************************
c
      implicit double precision (a-h,o-z)
      parameter (zip = 0.0d0, one = 1.0d0, two = 2.0d0)
      dimension x(il,im),t(il,im),con(il),alf(il),wid(il),n(il),
     +          a(il*im),b(il*im),c(il*im),f(il*im),z(il*im),dx(il),
     +          r(48),sr(48),tex(48),st(48),r1(il,im)
      logical shield
c
c     Open Input File
c
      open(unit = 15,file = 'sol.dat',status = 'old')
c
c     Read Input Data
c
      read(15,90)ill, t0, h, flux
c      write(*,*)ill, t0, h, flux
      if(ill.gt.il)then
        write(*,*)'Increase Parameter il'
        stop
      end if
      read(15,91)maxday, conv, dt, rout
c      write(*,*)maxday, conv, dt, rout
      read(15,96)ish,ec,es
c      write(*,*)ish
c
      if(ish.gt.0)then
        shield = .true.
```

```
      else
        shield = .false.
      end if
c
      do i = 1,ill
        read(15,92)n(i),wid(i),con(i),alf(i)
c        write(*,*)i,n(i),wid(i),con(i),alf(i)
        if(n(i)+1.ge.im)then
          write(*,*)'Increase Parameter im'
          stop
        end if
      end do
c
      read(15,*)
      read(15,*)
      do i = 1,24
        read(15,92)hour,r(i),tex(i)
        r(49-i) = r(i)
        tex(49-i) = tex(i)
c        write(*,*)i,r(i)
      end do
c
c     Get cosine FT of r -> sr, tex -> st
c
      pi = dacos(-one)
c
      do k = 1,48
        sr(k) = r(1) + r(48)*(-one**(k-1))
        st(k) = tex(1) + tex(48)*((-one)**(k-1))
        do j = 2,47
          sr(k) = sr(k) + two*r(j)*dcos(pi*dble((j-1)*(k-1))/47.0d0)
          st(k) = st(k) + two*tex(j)*dcos(pi*dble((j-1)*(k-1))/47.0d0)
        end do
c        write(*,*)k,sr(k),st(k)
      end do
      do k = 28,48
        st(k) = zip
      end do
c
c     Initialize Arrays
c
      nn = 0
      if(shield)then
        nn = 1
        tsh = t0
        a(nn) = zip
        b(nn) = zip
        c(nn) = zip
        f(nn) = zip
        z(nn) = zip
      end if
      xtemp = zip
      n(ill) = n(ill) - 1
      do i = 1,ill
```

```
      dx(i) = wid(i)/dble(n(i))
      do j = 1,n(i)
        nn = nn + 1
        x(i,j) = xtemp
        xtemp = xtemp + dx(i)
        r1(i,j) = zip
        t(i,j) = t0
        a(nn) = zip
        b(nn) = zip
        c(nn) = zip
        f(nn) = zip
        z(nn) = zip
      end do
    end do
    nn = nn + 1
    x(ill,n(ill)+1) = xtemp
    t(ill,n(ill)+1) = t0
    a(nn) = zip
    b(nn) = zip
    c(nn) = zip
    f(nn) = zip
    z(nn) = zip
c
    if(rout.gt.zip)then
      rtemp = rout
      do i = 1,ill
        do j = 1,n(i)
          r1(i,j) = one/rtemp
          rtemp = rtemp - dx(i)
        end do
      end do
      r1(ill,n(ill)+1) = one/rtemp
    end if
c
 90   format(///,1x,i9,4(1x,e14.7))
 91   format(//,1x,i9,3(1x,e14.7))
 92   format(1x,i9,3(1x,e14.7))
 96   format(//,1x,i9,2(1x,e14.7),//)
c
c
    end
c
c
c*********************************************************************
c
    subroutine proc(il,im,x,t,n,con,alf,wid,a,b,c,f,z,dx,nn,conv,
   +           maxday,dt,ill,h,flux,t24,tmin,tmax,sr,st,r1,shield,
   +           tsh,ec,es,tshmin,tshmax)
c
c*********************************************************************
c
    implicit double precision (a-h,o-z)
    parameter (two = 2.0d0,one = 1.0d0,zip = 0.0d0,huge = 1.0d10,
   +           day = 86.4d3, sig = 5.670d-8)
```

```
      dimension x(il,im),t(il,im),con(il),alf(il),wid(il),n(il),
     +  a(il*im),b(il*im),c(il*im),f(il*im),z(il*im),dx(il),
     +  t24(il,im),tmin(il,im),tmax(il,im),sr(48),st(48),r1(il,im)
      logical shield
c
c     Initialize Variables
c
      pi = dacos(-one)
      iter = 0
      res = huge
      iday = 0
      ish = 0
      if(shield)ish = 1
c      open(unit = 18,file = 'sol.spy',status = 'unknown')
c      write(18,*)
c
      do while (res.gt.conv.and.iday.lt.maxday)
c
        time = zip
        del = zip
        iday = iday + 1
c
c       Set tmin, tmax, t24
c
        tshmin = huge
        tshmax = -huge
        do i = 1,ill
          do j = 1,n(i)
            tmin(i,j) = huge
            tmax(i,j) = -huge
            t24(i,j) = t(i,j)
          end do
        end do
        tmin(ill,n(ill)+1) = huge
        tmax(ill,n(ill)+1) = -huge
c
        do while (time + dt/two.lt.day)
c
          open(unit = 16,file = 'sol.pro',status = 'unknown')
          iter = iter + 1
          time = time + dt
c          write(*,*) iday,time
c
c         Calculate Current Insolation, q, External Temperature, t8
c
          if(time.gt.3600.0d0)then
            qtime = time - 3600.0d0
          else
            qtime = time + 82800.0d0
          end if
c
          if(time.gt.14400.0d0)then
            ttime = time - 14400.0d0
          else
```

```
              ttime = time + 72000.0d0
            end if
c
            q = zip
            t8 = st(1)
            do j = 2,47
              q = q - sr(j)*dble(j-1)*dsin(pi*dble(j-1)*qtime/1.692d5)
              t8 = t8 + two*st(j)*dcos(pi*dble(j-1)*ttime/1.692d5)
            end do
            q = dmax1(q*pi/7952.4d0,zip)
            t8 = t8/(two*dble(48)-two)
c           write(*,*)q,t8
c
c           Calculate Coefficient Array
c
            if(shield)then
c       Shield
              co = one/es + one/ec - one
              b(1) = sig*(es*(tsh+t8)*(tsh*tsh+t8*t8) +
     +                co*(tsh+t(1,1))*(tsh*tsh+t(1,1)*t(1,1))) + h
              c(1) = -sig*co*(tsh+t(1,1))*(tsh*tsh+t(1,1)*t(1,1))
              f(1) = q + sig*es*t8*(tsh+t8)*(tsh*tsh+t8*t8) + h*t8
c       Outer Node
              dx2 = dx(1)*dx(1)/8.0d0/dt/alf(1)
              a(2) = -sig/con(1)*co*(tsh+t(1,1))*(tsh*tsh+t(1,1)*t(1,1))
              b(2) = (two/dx(1) - r1(1,1))/two
     +             + sig/con(1)*co*(tsh+t(1,1))*(tsh*tsh+t(1,1)*t(1,1))
     +             + dx2*(4.0d0/dx(1) - r1(1,1))
              c(2) = -(two/dx(1) - r1(1,1))/two
              f(2) = dx2*(4.0d0/dx(1) - r1(1,1))*t(1,1)
            else
c       Outer Node
              dx2 = dx(1)*dx(1)/8.0d0/dt/alf(1)
              b(1) = (two/dx(1) - r1(1,1))/two + h/con(1)
     +             + dx2*(4.0d0/dx(1) - r1(1,1))
     +             + sig*ec/con(1)*(t(1,1)+t8)*(t(1,1)*t(1,1)+t8*t8)
              c(1) = -(two/dx(1) - r1(1,1))/two
              f(1) = (q + h*t8)/con(1)
     +             + dx2*(4.0d0/dx(1) - r1(1,1))*t(1,1)
     +             + sig*ec/con(1)*t8*(t(1,1)+t8)*(t(1,1)*t(1,1)+t8*t8)
            end if
c       Inner Node
            dx2 = dx(ill)*dx(ill)/8.0d0/dt/alf(ill)
            a(nn) = -(two/dx(ill) + r1(ill,n(ill)+1))/two
            b(nn) = (two/dx(ill) + r1(ill,n(ill)+1))/two
     +           + dx2*(4.0d0/dx(ill) + r1(ill,n(ill)+1))
            f(nn) = flux/con(ill) + dx2*(4.0d0/dx(ill)
     +           + r1(ill,n(ill)+1))*t(ill,n(ill)+1)
c       Interface Nodes
            m = 1 + ish
            do i = 1,ill-1
              m = m + n(i)
              rc = (con(i)*dx(i)/alf(i) + con(i+1)*dx(i+1)/alf(i+1))
     +             /(dx(i) + dx(i+1))/dt
```

```
            dx2 = one/(dx(i)+dx(i+1))
            a(m) = -con(i)*dx2*(two/dx(i) + r1(i,1))
            b(m) = dx2*(con(i+1)*(two/dx(i+1) - r1(i,1))
     +                 + con(i)*(two/dx(i) + r1(i,1))) + rc
            c(m) = con(i+1)*dx2*(-two/dx(i+1) + r1(i,1))
            f(m) = t(i+1,1)*rc
          end do
c       Interior Nodes
          m = ish
          do i = 1,ill
            m = m + 1
            do j = 2,n(i)
              m = m + 1
              dx2 = dx(i)*dx(i)/alf(i)/dt
              a(m) = r1(i,j)*dx(i)/two - one
              b(m) = two + dx2
              c(m) = -r1(i,j)*dx(i)/two - one
              f(m) = t(i,j)*dx2
            end do
          end do
c
c         Solve Tri-Diagonal Matrix
c
          call trid(nn,a,b,c,f,z)
c
c         Store New Temperatures
c
          if(shield)then
            del = dmax1(del,dabs(tsh-z(1)),dabs(t(1,1)-z(2)))
            tsh = z(1)
            tshmin = dmin1(tsh,tshmin)
            tshmax = dmax1(tsh,tshmax)
          end if
          m = ish
          do i = 1,ill
            do j = 1,n(i)
              m = m + 1
c              write(*,*)i,j,t(i,j),z(m)
              t(i,j) = z(m)
              tmax(i,j) = dmax1(t(i,j),tmax(i,j))
              tmin(i,j) = dmin1(t(i,j),tmin(i,j))
            end do
          end do
          t(ill,n(ill)+1) = z(nn)
          tmax(ill,n(ill)+1)=dmax1(t(ill,n(ill)+1),tmax(ill,n(ill)+1))
          tmin(ill,n(ill)+1)=dmin1(t(ill,n(ill)+1),tmin(ill,n(ill)+1))
          write(16,94)day*dble(iday-1)+time,t8,tsh,(t(i,1),i=1,ill),
     +                t(ill,n(ill)+1)
c         write(*,*)t(ill,n(ill)+1),tmin(ill,n(ill)+1),
c    +              tmax(ill,n(ill)+1)
c         if(iday.ge.115)then
c           do i = 1,ill
c             do j = 1,n(i)
c               write(18,97)time,x(i,j),t(i,j)
```

```
c              end do
c            end do
c            write(18,97)time,x(ill,n(ill)+1),t(ill,n(ill)+1)
c          end if
c
          end do
c
c         Check for Convergence
c
          res = zip
          do i = 1,ill
            do j = 1,n(i)
              de = t(i,j) - t24(i,j)
              res = dmax1(res,dabs(de))
c              write(*,*)i,j,t(i,j),t24(i,j)
            end do
          end do
          write(*,93)iday,res
          close(16)
c
        end do
c        close(18)
        write(*,*)'Maximum Surface Temperature Change = ',del
c
 93     format(3x,i6,3x,e14.7)
 94     format(9(1x,e14.7))
 97     format(3(3x,e13.6))
c
c
        return
        end
c
c
c*************************************************************************
c
        subroutine post(il,im,x,t,n,tmin,tmax,ill,tshmin,tshmax)
c
c*************************************************************************
c
        implicit double precision (a-h,o-z)
        parameter (two = 2.0d0,one = 1.0d0,zip = 0.0d0)
        dimension x(il,im),t(il,im),n(i),tmin(il,im),tmax(il,im)
c
        open(unit = 17,file = 'sol.out',status = 'unknown')
c
        write(17,95)-one,tshmin,tshmax
        do i = 1,ill
          do j = 1,n(i)
            write(17,95)x(i,j),tmin(i,j),tmax(i,j)
          end do
        end do
        write(17,95)x(ill,n(ill)+1),tmin(ill,n(ill)+1),
     +              tmax(ill,n(ill)+1)
c
```

```
 95   format(3(3x,e14.7))
c
c
      return
      end
c
c
c**********************************************************************
c
      subroutine trid(im,a,b,c,f,z)
c
c**********************************************************************
c
      implicit double precision (a-h,o-z)
c
      parameter (ii = 500)
      dimension a(im),b(im),c(im),f(im),z(im),wks(ii)
c
      if(ii.lt.im)then
        write(*,*)' ii too small in trid'
        stop
      end if
      bet = b(1)
      z(1) = f(1)/bet
c      write(*,*)a(1),b(1),c(1),f(1)
      do i = 2,im
c        write(*,*)a(i),b(i),c(i),f(i)
        wks(i) = c(i-1)/bet
        bet = b(i)-a(i)*wks(i)
        z(i) = (f(i) - a(i)*z(i-1))/bet
      end do
c
      do i = im-1,1,-1
        z(i) = z(i) - wks(i+1)*z(i+1)
      end do
c
c
      return
      end
```

APPENDIX B: INPUT FILE LISTING

Input data for Insolation Code

layers	initial t	conv coeff	interior flux
5	+4.3000000e+02	+1.0000000e+01	+1.0000000e+02

max days	convergence	time step	cask out rad
1000	+1.0000000e-02	+0.0100000e+03	+5.3261260e-01

shield ?	cask emisivity	shield emsivty
1	+3.0000000e-01	+1.0000000e-00

# of nodes	width	conductivity	diffusivity
25	+3.1750000e-03	+1.3849400e+01	+3.8128850e-06
50	+9.3980000e-02	+1.4535000e-01	+8.0212010e-08
50	+3.8100000e-02	+1.3849400e+01	+3.8128850e-06
50	+5.3848000e-02	+2.5539400e+01	+1.0039860e-05
25	+9.5250000e-03	+1.3849400e+01	+3.8128850e-06

hour	radiation	temperature
1	+0.0000000e+00	+3.0520000e+02
2	+0.0000000e+00	+3.0470000e+02
3	+0.0000000e+00	+3.0410000e+02
4	+0.0000000e+00	+3.0470000e+02
5	+1.3000000e+01	+3.0630000e+02
6	+3.5200000e+02	+3.0860000e+02
7	+1.4770000e+03	+3.0970000e+02
8	+3.4520000e+03	+3.1190000e+02
9	+6.2390000e+03	+3.1470000e+02
10	+9.5990000e+03	+3.1630000e+02
11	+1.3390000e+04	+3.1740000e+02
12	+1.7436000e+04	+3.1860000e+02
13	+2.1490000e+04	+3.1930000e+02
14	+2.5256000e+04	+3.1800000e+02
15	+2.8582000e+04	+3.1740000e+02
16	+3.1389000e+04	+3.1410000e+02
17	+3.3439000e+04	+3.1240000e+02
18	+3.4585000e+04	+3.0970000e+02
19	+3.4945000e+04	+3.0800000e+02
20	+3.4958000e+04	+3.0630000e+02
21	+3.4958000e+04	+3.0630000e+02
22	+3.4958000e+04	+3.0410000e+02
23	+3.4958000e+04	+3.0470000e+02
24	+3.4958000e+04	+3.0520000e+02

DISTRIBUTION

1 Tom Doering
B&W Fuel Company
Waste Package Design
101 Convention Center Dr., Suite 540
Las Vegas, NV 89109

5 William Lake
U.S. Department of Energy, RW-431
Forrestal Building, 7F-052
1000 Independence Avenue SW
Washington, DC 20585

3 TRW Environmental Safety Systems Inc.
Attn: D. J. Nolan
M. Rahimi
M. Pakstys
2650 Park Tower Drive, Suite 800
Vienna, VA 22180

162 U.S. Department of Energy
Office of Scientific and Technical Information
Attn: DOE/OSTI-4500-R74UC-722
Oak Ridge, TN 37830

4 U.S. Department of Energy
Attn: R. Brancato, EM-56
D. Lillian, EM-56
L. Blalock, EM-561
E. McNeil, EM-561
Mail Stop EM-561
Washington, DC 20545

2 U.S. Department of Energy
Albuquerque Operations Office
Albuquerque Headquarters
Attn: K. G. Golliher
D. Bandy
P.O. Box 5400
Albuquerque, NM 87115

4 U.S. Nuclear Regulatory Commission
Office of Nuclear Material Safety and Safeguards
Attn: R. Chappell
H. Lee
Washington, DC 20555

1 Jeff Williams
U.S. Department of Energy, RW-421
Forrestal Building, 7F-059
1000 Independence Avenue SW
Washington, DC 20585

10	MS0835	1513	S. E. Gianoulakis
1	MS0835	1513	R. D. Skocypec
1	MS0726	6600	J. B. Woodard
1	MS0715	6603	R. E. Luna Attn: TTC Master File
25	MS0715	6603	TTC Library
1	MS0717	6642	G. F. Hohnstreiter
1	MS0717	6642	D. C. Harding
1	MS0716	6643	M. C. Brady
5	MS0899	7141	Technical Library
1	MS0619	7151	Technical Publications
10	MS1119	7613-2	Document Processing for DOE/OSTI
1	MS9018	8523-2	Central Technical Files

DATE
FILMED
8/9/94
END